Engineering Structures 289 (2023) 116243

Contents lists available at ScienceDirect

Engineering Structures

journal homepage: www.elsevier.com/locate/engstruct

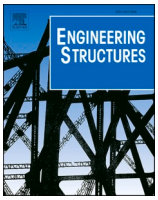

Design and testing of a decision tree algorithm for early failure detection in steel truss bridges

B. Barros, B. Conde, M. Cabaleiro, B. Riveiro *

CINTECX, Universidade de Vigo, GeoTECH Group, Campus Universitario de Vigo, As Lagoas, Marcosende, 36310 Vigo, Spain

ARTICLE INFO

Keywords:
Damage identification
Model-based decision tree algorithm
Riveted steel truss bridge
Ambient vibration test
FE model updating

ABSTRACT

This paper develops a methodology for damage identification in steel truss bridges that uses vibration-based monitoring data and a model-based decision tree algorithm. The methodology resorts to a calibrated FE model with an optimization-based parameter identification procedure to simulate and analyze all the potential damages that might affect the structure. The effect of environmental conditions on the modal parameters is also accounted for, which is modeled as structure stiffness variations using the Young's modulus and forecasted using a surrogate modeling strategy. The feasibility of the methodology is demonstrated on a full-scale bridge in Vilagarcía de Arousa, Spain. The underlying hypotheses used in the algorithm implementation were validated, and the error ponderation and selection bound employed to detect and identify damage were optimized. The results show an average success rate of 95.0% and an average false positive rate of 1.0% in identifying damage indicating its robustness to be extrapolated to other case studies.

1. Introduction

Bridges are one of the most critical assets in the transport network. They entail high social, economic, and even political impacts. Investment in transport and infrastructure achieves an important part of the Gross Domestic Product of the most advanced countries. In the 19 EU Member States, this rate achieves an average of the 1.1% [1]. However, reports about the state of infrastructure tell us that infrastructure budgets are insufficient. Nowadays, in EEUU, 42% of the bridges are at least 50 years old, and 46,154 (7.5%) are considered structurally deficient. Estimates show that it is necessary to increase the annual budget for the rehabilitation of bridges from $14.4 billion to $22.7 billion (58%) [2]. Regarding the railway in Europe, it is estimated that 1500 bridges are expected to be strengthened in the next ten years, 3000 have to replace their deck, and 4500 have to be entirely replaced [3]. The risk associated with this generalized lack of maintenance is very high. Only in China, more than 300 bridges collapsed, with 564 fatalities and 917 injuries between 2000 and 2014 [4]. Over 500 bridges collapsed in EEUU between 1989 and 2000, with an average age of 52.5 years [5]. Europe has also experienced major bridge collapses, such as the Entre-os-Rios bridge in Portugal, where 59 people died [6], or the more recent Polcevera Viaduct in Italy, where 43 people died [7].

Due to the serious consequences of these collapses and the aging of the global inventory of infrastructure, the great importance of maintenance tasks and routine inspections to anticipate collapses is highlighted. In this sense, the case of the bridge of the northwest highway (A6) in Spain is remarkable, which was closed in September 2021 after detecting a failure in one of the inspection and maintenance tasks. However, despite the efforts to repair it (about €25 million), the bridge collapsed on June 7, 2022, without losing human lives [8]. This event confirms that bridges had to be periodically summited to robust maintenance tasks and inspections to ensure their correct state. Usually, these inspections are based only on a visual inspection where the experience of the technicians is essential. Structural Health Monitoring (SHM) could greatly support these inspection tasks and make the procedure more robust and efficient. The statistics on bridge failures from 2009 to 2019 in China show that most are related to anthropic factors (69.6%) [9]. Generally, this type of collapse can be avoided or mitigated with structural health monitoring, risk assessment, and suitable management systems.

During recent decades, the safety and the optimization of inspection costs have become top priorities for the civil engineering community of practice and researchers. Since the beginning of this century, cost-effective structural health monitoring (SHM) to ensure long-term structural integrity and safety levels has been highlighted on many platforms [10]. Many different SHM methods have been proposed to

* Corresponding author at: CINTECX, Universidade de Vigo, GeoTECH Group, Campus Universitario de Vigo, As Lagoas, Marcosende, 36310 Vigo, Spain.
E-mail address: belenriveiro@uvigo.gal (B. Riveiro).

https://doi.org/10.1016/j.engstruct.2023.116243
Received 30 December 2022; Received in revised form 27 April 2023; Accepted 28 April 2023
Available online 18 May 2023

modernize periodic inspections and minimize the consequences of undesired failure of aging infrastructure. Among others, non-destructive (NDT) active or passive testing techniques (e.g., impact echo, ultrasonic surface wave, ground-penetrating radar, electrical resistivity) [11], IoT [12] and sensor systems (such as Fiber Optic Sensors (FOS) [13,14] or bridge weight-in-motion (BWIM) [15–17]), and remote-sensing based dedicated inspection platforms (e.g., vehicle-borne laser scanning, UAV, IR-thermography) [18–21] have been deeply investigated in the last two decades. Recent advancements in sensor and communication technologies (contact and contactless, wired and wireless, etc.) have created opportunities for the acquisition of sensor data (observable response) at an unprecedented rate and amount. These advances, together with the increasing concern about frequent extreme events, motivated the extensive deployment of sensor networks by civil infrastructure owners and operators during the last years, easing that large amounts of heterogeneous data become available from various sensors.

Most of the SHM methods proposed can be classified into two main broad categories: vision-based and vibration-based methods. The vision-based methods mainly focus on detecting and parametrizing signs of malfunctioning or damage from imagery of different nature (RGB images, 3D point clouds, IR Thermography, etc.). These approaches are probably the ones that most rapidly adopt the advances in artificial intelligence (AI), as it directly benefits from the radical developments in autonomous image processing tools proposed in other fields. An extensive review of vision-based SHM was presented in [22,23], where crack detection, change detection, and corrosion are among the most typical applications reported in the literature. However, the relation between detecting these local damages to the global response of the structure is limited.

In vibration-based SHM methods, the direct benefit from advances in other computer vision domains is not so straightforward; however, vibration-based methods have the advantage that they are built on the premise that damages (physical changes) cause the corresponding changes in the global vibration response of the structure (i.e., natural frequencies and mode shapes) [24,25]. These methods have been widely investigated as they represent a suitable means of accurately assessing structural safety. In this context, vibration-based SHM methods are classified into two main categories: model-based (parametric) and non-model-based (non-parametric). The model-based approach uses a numerical model of the structure (e.g., based on the finite element method (FEM), that evaluates the inconsistencies between the measured and model-generated (simulated) data for damage identification. These techniques require advanced computational models and associated assumptions about the structural system as these are solving the physical model. These approaches give good accuracy, but the uncertainties about the structural system reduce their use in real applications. Non-parametric methods (data-driven) are a good alternative when reliable computational models cannot be developed. These models essentially perform post-processing of response (sensor) data to identify damages without any prior assumption regarding the structural system. Data-driven approaches are where AI has most noticeably impacted. In this sense, Pattern Recognition is used in SHM applications with the goal of classifying objects based on patterns represented by a set of features using concepts from statistical decision theory. The most common use in structural engineering has been for SHM and damage identification [22,26]. Machine Learning (ML) is a subfield of AI dealing with studying, designing, and developing algorithms that can learn from the data and make predictions using learned data [27]. ML methods have been increasingly adopted over the last decade due to their enormous capability to map the relations among input and output data that are non-linear or complicated to formulate mathematically. Many SHM applications include damage detection, structural reliability, and parameter identification [28,22,29].

Continuous monitoring has shown to be especially useful for real-time control and management of in-service systems, aiming to anticipate failures or at least minimize their consequences. However, the vast stock of in-service bridges and the high cost of these systems make it challenging to deploy monitoring systems massively. For instance, according to the national bridge inventory, only in EEUU there are more than 690.000 bridges [5], while in Europe, the estimations round 1 million of bridges [3]. Current state budgets assigned to structural maintenance constrain the adoption of continuous monitoring in most of the bridge stock. Only those most critical bridges are equipped with advanced monitoring systems, and the others remain subject to traditional routine inspections. However, the use of discrete monitoring to complement the traditional routine inspections could be a solution to increase the number of monitored bridges due to its lower cost. Discrete monitoring allows the shared use of the monitoring equipment, thus requiring a smaller budget to be implemented. This methodology can also improve the knowledge about the condition state of the bridge through the comparison of the actual dynamic behavior of the bridge along successive inspections. If there are any damaged elements in the bridge, the dynamic behavior of the structure will change, affecting its modal properties. Sometimes these initial failures are not detected in routine inspections because of human error or because they are not detectable to the eyes of inspectors. For this reason, including dynamic monitoring in routine inspections offers opportunities to detect initial failures accurately, thus preventing the collapse of the structure.

In this work, a model-based decision tree algorithm is proposed to work as an early damage predictor of steel truss bridges using periodic monitoring data (continuous or discrete). This approach aims to automate the inspection and monitoring tasks in steel truss bridges in a robust manner. The methodology is based on a model-based approach that employs an accurate calibrated FE model to determine the effect of various potential damages in the bridge. Accordingly, a selection of potential damages is considered, constituting the predictive objectives of the algorithm. It is noted that not contemplated damage scenarios, such as settlements and loss of stiffness in supports or connections, are potential damages of a more complex nature that require specific studies. Thus, they can only be detected as possible damage through changes in the modal properties of the structure, yet they will not be identified. The designed decision tree algorithm is used to evaluate all the potential damages selected and predict if: i) there is damage in the structure and ii) which is the most probable damaged element. The methodology was implemented in a steel truss bridge in Vilagarcía de Arousa (Spain). In the following sections, the workflow adopted, the architecture of the algorithm, and its implementation are explained in detail. Finally, the conclusions obtained are presented in Section 6.

2. Methodology

2.1. Application workflow

The proposed algorithm is designed to be implemented within a methodology that comprises three stages: I) Initial inspection, II) Routine inspection, and III) Damage prediction, as it is illustrated in Fig. 1.

I) Initial inspection: The initial inspection of the bridge consists of an experimental campaign aimed at collecting all the necessary data to create the FE model of the structure. In this campaign, an Ambient Vibration Test (AVT) is also performed to determine the initial modal parameters of the case study. Once all the experimental data is collected, the FE model is designed and refined to create an accurate numerical model. The model is finally updated using an optimization-based parameter identification procedure. This operation reduces the uncertainty of the FE model and ensures that it accurately represents the actual response of the structure. The next step consists of designing the different potential damages that the structure may suffer. With these potential damages adequately designed, the assumed hypotheses are validated. Finally, a synthetic dataset with several damage scenarios will be created using combinations of potential damages in order to optimize

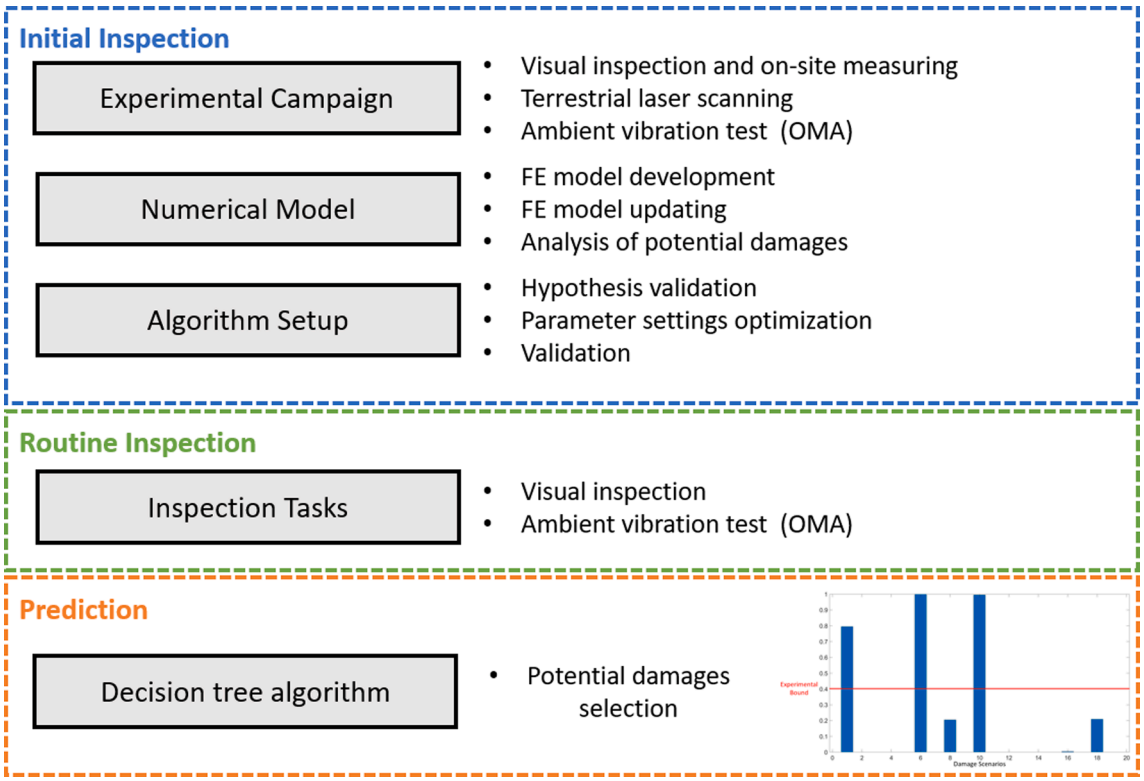

Fig. 1. Outline of the steps of the proposed methodology.

the response of the algorithm in the case study using a genetic algorithm, as depicted in section 5.5. The modal properties of the generated dataset will be contaminated with Gaussian noise to reproduce the effect of environmental conditions. Once the setting parameters of the algorithm are optimized, the early damage-predicting algorithm is ready to be applied to the data extracted from the routine inspection.

II) Routine inspection: In the following monitoring campaign, in addition to the required survey tasks, the Ambient Vibration Test (AVT) is repeated, and thus new modal parameters are obtained.

III) Prediction: The actual modal properties measured in the routine inspection are introduced as inputs to be predicted in the decision tree algorithm. The output of the algorithm includes not only the presence of damage but also the most likely damaged elements that trigger the detected changes in the modal properties.

2.2. Initial hypothesis

The proposed algorithm is designed under the following assumptions:

I) Hypothesis of damage differentiation: Each structural element has a serial of features (geometry, localization, etc.) that provide stiffness to the structure in a specific manner. Therefore, their deterioration will cause different changes in the modal properties of the bridge. This fact provokes different residual components for each potential damage, thus allowing their identification when the algorithm is applied.

II) Hypothesis of additivity: This assumption states that the influence of a potential damage on the prediction is independent of any other damage. This means that potential damages can be designed additively so that they can act simultaneously without causing inconsistencies in the prediction. Thus, it should be verified that the sum of the effects of the potential damages is cumulative and does not present highly nonlinear interactions. If this were the case, the algorithm would need to evaluate the FE model for each iteration of the decision tree, which would considerably increase the computational cost. Another possible approach would be using metamodels to reduce computational time; however, this implies using, e.g., deep learning techniques capable of mapping these high nonlinearities. Finally, to avoid changes in the modal parameters that cannot be identified, the potential damages must represent all damage possibilities of the structure, considering all constituent elements. This hypothesis will be studied and validated in the algorithm setup.

2.3. Architecture of the decision tree algorithm

The structure of the tree algorithm starts from a root which represents the modal properties of the structure in the initial or previous routine inspection. This root node is linked to some children nodes, which represent the first layer of the algorithm. In this first layer, the changes in the modal properties provoked by different environmental conditions are added to the initial values. Consequently, a set of children nodes will be the starting points for the algorithm. The number of children nodes (S) is a parameter to be optimized in the algorithm setup and depends on the bridge's conditions. Once the children nodes of the first layer are estimated, the algorithm builds a subtree structure that evaluates the potential damages. The depth of the subtree structure (number of layers) will depend on the nature of the damage scenario, i.e., the number of actual damages and its noise level. The leaf nodes of the subtree structure are used to select and quantify the most likely potential damages. Finally, an indicator summarizes the concurrency of each potential damage in predicting the damage scenario. The workflow of the algorithm is depicted in Fig. 2.

2.3.1. Damage indicator

To predict the damage scenarios, a Damage Indicator (DI) was adopted that quantifies the differences in the modal properties. This DI will be used at each node of the tree structure to quantify the differences between the current node values and those obtained in the routine inspection (DI_{node}). Besides, the same DI is also employed to quantify the differences between the current and the previous inspection (DI_{CI}). The potential damage that minimizes the difference between both DI will be

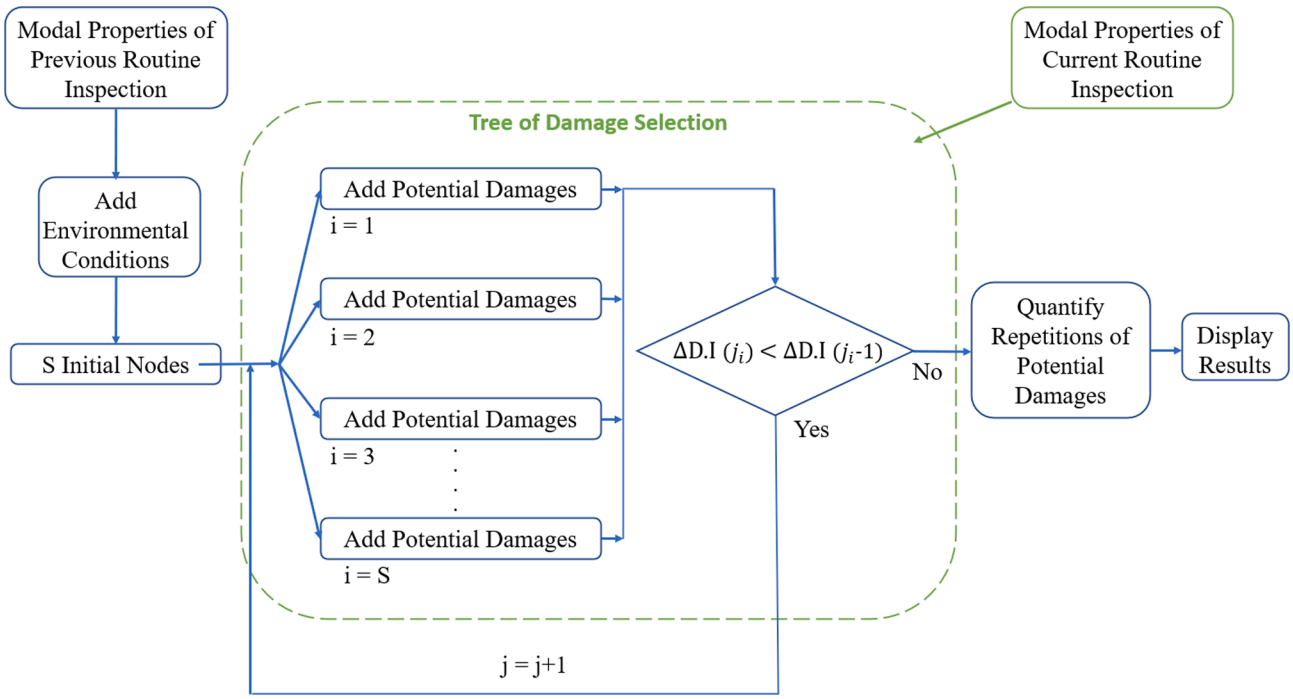

Fig. 2. Workflow of the decision tree algorithm.

chosen for the next iteration ($\Delta DI = DI_{CI} - DI_{node}$). The function chosen as DI is composed of two different terms. The first quantifies the difference in natural frequencies. The second quantifies the difference in modal displacements using the Modal Assurance Criterion (MAC) [30], which is the normalized scalar product of two sets of vectors $\{\varphi_A\}$and $\{\varphi_X\}$ in order to check its orthogonality; as shown in Equation (1).

$$MAC(r,q) = \frac{\left|\{\varphi_A\}_r^T\{\varphi_X\}_q\right|^2}{\left(\{\varphi_A\}_r^T\{\varphi_A\}_r\right)\left(\{\varphi_X\}_q^T\{\varphi_X\}_r\right)} \tag{1}$$

The DI function is a simplified version of the classic error function used in single-objective optimization-based model updating processes and is given in Equation (2):

$$DI = \left[\sum_{i=1}^{m}\left(\frac{\mathscr{F}_i^{case} - \mathscr{F}_i^0}{\mathscr{F}_i^0}\right) + \sum_{i=1}^{m}\left(\frac{MAC_i^{case} - MAC_i^0}{MAC_i^0}\right)\right] \tag{2}$$

where m is the number of vibration modes considered, $\mathscr{F}_i^0$ is the $i-th$ natural frequency of the previous routine inspection (obtained in the AVT) and MAC_i^0 is the MAC between the modal displacements of the updated FE model and the experimental results for the $i-th$ vibration mode. In the case of computing DI_{node}, $\mathscr{F}_i^{case}$ represents the frequency of the previous inspection plus the effects of the selected potential damages and MAC_i^{case} is the modal assurance criterion between the experimental results of the previous inspection and the updated FE model plus the effects of the selected potential damages. In the case of computing DI_{CI}, $\mathscr{F}_i^{case}$ is the natural frequency of the current inspection and MAC_i^{case} is the MAC value between the current and the previous inspection.

2.3.2. Tree of damage selection

As explained above, the decision tree starts with the root node representing the natural frequencies obtained from the AVT and the MAC between the experimental and numerical modal displacements (updated FE model). It should be noted that changes in modal properties may occur due to variations in environmental conditions. As these variations may lead to confusion in predicting the damage scenarios, the first step consists of estimating the effects of environmental conditions on modal parameters. Thus, Equation (3) was employed to estimate the relation between the temperature and the Young's modulus, which was developed in [31] and used in other works such as [32]. This equation computes the Young's modulus variation of structural steel depending on the temperature in a variation range of 0 °C < T < 600 °C.

$$\begin{aligned} E(T)) &= e_0 + e_1T + e_2T^2 + e_3T^3 \\ e_0 &= 206GPa \\ e_1 &= -4.326X10^{-2}GPa/^oC \\ e_2 &= -3.502X10^{-5}GPa/^oC \\ e_3 &= -6.592X10^{-8}GPa/^oC \end{aligned} \tag{3}$$

Besides temperature, other meteorological variables, such as humidity and wind speed, may affect the estimated modal parameters from the AVT. These variables also affect the structure globally. The effect of wind can be modeled as a distributed load on the structure, while other parameters, such as humidity or temperature, can be modeled as structure stiffness variations using the Young's modulus. However, these effects may be increased due to damage, stress concentration, or the deteriorated condition of the connection of some elements, among others. Therefore, it is advisable to use a Safety Coefficient (SC) that can consider the effect of all sources of uncertainty. Once the SC is established by attending to the singularities of the case study, a variation range for the different parameters (e.g., Young's modulus) employed to represent the effects of environmental conditions is obtained. Thus, the nodes of the first layer of the algorithm are created, which will adopt equidistant values covering the whole variation range to compute the frequencies and MACs corresponding to the different environmental conditions.

To compute the modal properties of each node, the FE model is replaced by a surrogate model to avoid the high computational cost. The surrogate model was built using the Kriging methodology [33], which approximates the FE model response $M^K(\boldsymbol{x})$ for a set of inputs ($\mathbf{x}$), see

Equation (4) [34].

$$M^K(\boldsymbol{x}) = \sum_{j=1}^{p} f_j(\boldsymbol{x})\beta_j + Z(\boldsymbol{x}) = \boldsymbol{f}^T(\boldsymbol{x})\boldsymbol{\beta}(\boldsymbol{x}) + Z(\boldsymbol{x}) \quad (4)$$

The trend of the Gaussian process is represented by the term $\boldsymbol{f}^T(\boldsymbol{x})\boldsymbol{\beta}(\boldsymbol{x})$, which consists of P arbitrary functions $\{f_j; j = 1, \ldots, P\}$ and their corresponding coefficients $\{\beta_j; j = 1, \ldots, P\}$. $Z(\boldsymbol{x})$ represents a stochastic process that is composed of a constant variance (σ^2), and a zero-mean, unit-variance stationary Gaussian process ($Z(\boldsymbol{x}, \omega)$) as per Equation (5) [35].

$$Z(\boldsymbol{x}) = \sigma^2 Z(\boldsymbol{x}, \omega) \quad (5)$$

being ω the probability space defined by the correlation function $R = R(\boldsymbol{x}, \boldsymbol{x}'; \boldsymbol{\theta})$, and $\boldsymbol{\theta}$ hyperparameters estimated by means of an optimization process. The surrogate models are trained based on datasets generated with the calibrated FE model. Space-filling sampling techniques, such as the Latin Hypercube Sampling (LHS) [36], are recommended to generate the training datasets. Once the metamodel is built, the algorithm can be used for prognosing the impact of environmental conditions.

The number of nodes of the first layer (children) is given by the variable *S*, and its value is related to the prediction of the environmental conditions and is determined at the validation stage by performing a parametric analysis. At the same time, every child node is used as a starting point in the subtree structure to select the potential damages, as depicted in Fig. 3.

2.3.3. Subtree structure

Starting from the first layer of nodes, the algorithm evaluates the effect of all potential damages on the structure. From this evaluation, the algorithm selects the *N* damages that produce the lowest difference between the Damage Indicator (DI) of the node and the damage scenario to be predicted. These will create the *N* nodes of the second layer of the algorithm. Starting from these *N* nodes, the algorithm will repeat the damage evaluation process, selecting the *N* best cases. This process will be repeated until the DI residual between the node and the damage scenario to be predicted is minimized. The residual is considered to be minimized when the addition of any of the unselected potential damages at the current node increases its value. Each end of the branch will be saved as a final node called a leaf node. Exemplary, Fig. 4 highlights the leaf nodes obtained by the subtree structure from one of the nodes of the first layer (starting points) for a number of paths $N = 2$.

Once all branches of the tree structure have been made, the result is a vector of leaf nodes.

$\boldsymbol{f} = \{f_i; i = 1, \ldots, n\}$ whose length (n) depends on the characteristics of the damage scenario to be predicted. The number of simultaneous damages identified within each leaf node is given by the number of iterations $\boldsymbol{j} = \{j_i; i = 1, \ldots, n\}$ that are needed to minimize the Damage Indicator (DI) residual (depth of the subtree structure). All selected potential damages are then clustered in the matrix $\boldsymbol{S}$ with dimensions $n \times j_{max}$, where j_{max} is the maximum depth (i.e., number of iterations) in the set of leaf nodes ($\max(\boldsymbol{j})$). In each vector $\boldsymbol{S}_i$ of the matrix $\boldsymbol{S}$, the potential damages identified for the leaf node f_i are listed, and the remaining positions ($j_{max} - j_i$) are filled with zeros, indicating no damage.

Subsequently, the matrix $\boldsymbol{Q}$ with dimensions $n \times \lambda$ (where λ is the total number of potential damages) is created to represent the set of damages selected in each leaf node in order to quantify their recurrence and thus obtain their final number of observations. For this purpose, a sigmoid function was used to evaluate whether each potential damage z is present in the clustered damages (S_i) of the leaf node i. If the potential

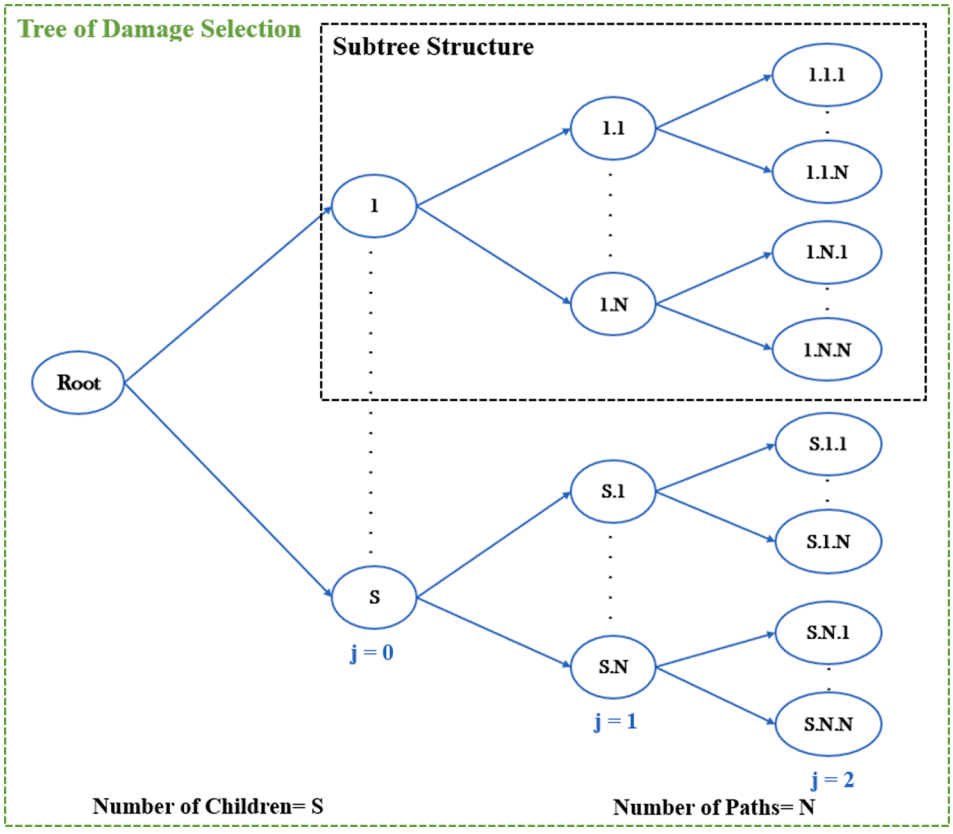

Fig. 3. Graphic representation of the workflow of the subtrees of potential damages selection.

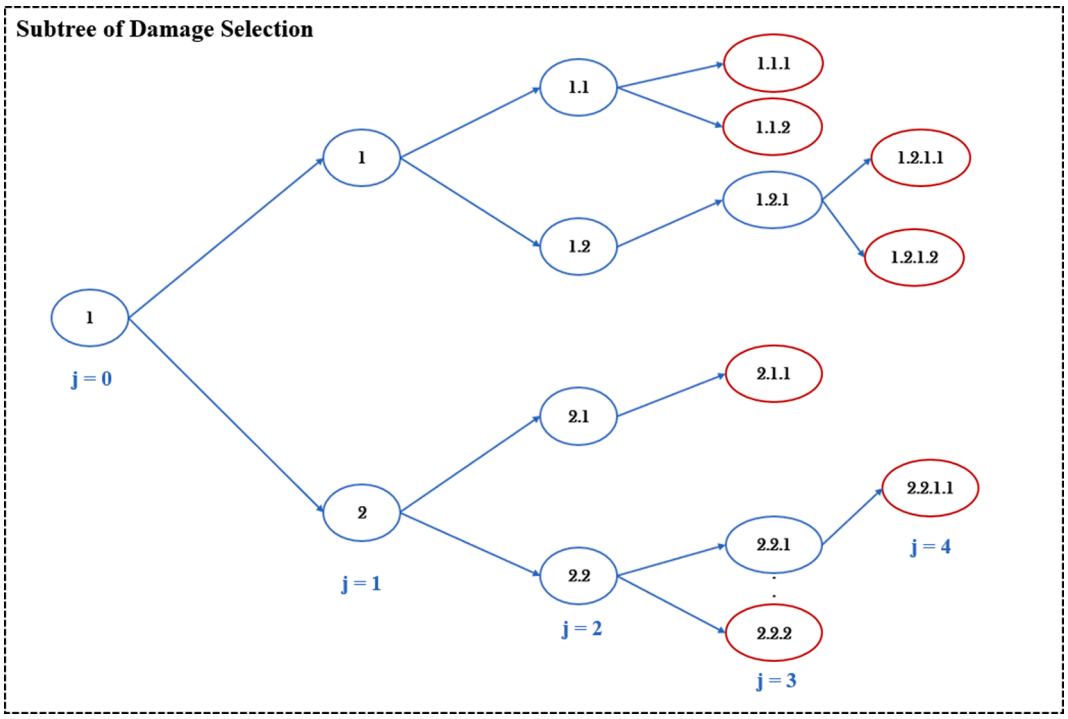

Fig. 4. Example of a prediction branch for a number of paths $N = 2$; the leaf nodes are highlighted in red. (For interpretation of the references to colour in this figure legend, the reader is referred to the web version of this article.)

damage z is present, the value of the matrix $\boldsymbol{Q}$ at row i and column z is 1; otherwise, it takes the value 0, see Equation (6):

$$\boldsymbol{Q}_{(i,z)} = \left\{ \begin{array}{l} 1 \text{ if Potential damage}_z \in \boldsymbol{S}_i \\ 0 \text{ if Potential damage}_z \notin \boldsymbol{S}_i \\ \quad 1 \le z \le \lambda \\ \quad 1 \le i \le n \end{array} \right\} \tag{6}$$

This methodology extracts the set of damages identified within each leaf node $\boldsymbol{Q}_{(i,z)}$ and computes the probability rate of each potential damage z. This adds robustness to the algorithm by evaluating all possible damage combinations but also leads to false positives. To overcome this drawback, it was decided to weight each potential damage z based on the normalized DI residual value of the corresponding leaf node f_i. For this purpose, the differences between the DI of the damage scenario to be predicted and the corresponding leaf node were obtained; this difference is represented by the vector of residuals $\boldsymbol{r} = \{r_i; i = 1, \ldots, n\}$. These residuals were then normalized between 0 and 1 with respect to the maximum and minimum values to obtain the set of normalized residual values $\{res_i; i = 1, \ldots, n\}$, which were finally used to weight the $\boldsymbol{Q}$ matrix.

However, due to the enormous number of damage combinations covered in each prediction, the exponential factor K has been added to increase the weighting of the normalized DI residual value of each leaf node f_i. This factor K should be optimized depending on the case study to be analyzed, since it depends on the characteristics of each particular case, such as the number of potential damages considered, the differentiability between them, the maximum number of damages applied simultaneously, etc.). Once the factor K is optimized, the probability of each potential damage $P(PotentialDamage(z))$ is calculated as the sum of the damage quantification $\boldsymbol{Q}_{(i,z)}$ over the total number of leaf nodes (n) and weighted by the expression $(1 - \boldsymbol{res}_i)^{*}10^{K}$, where $\boldsymbol{res}_i$ is the normalized residual of each leaf node f_i. The result is the weighted

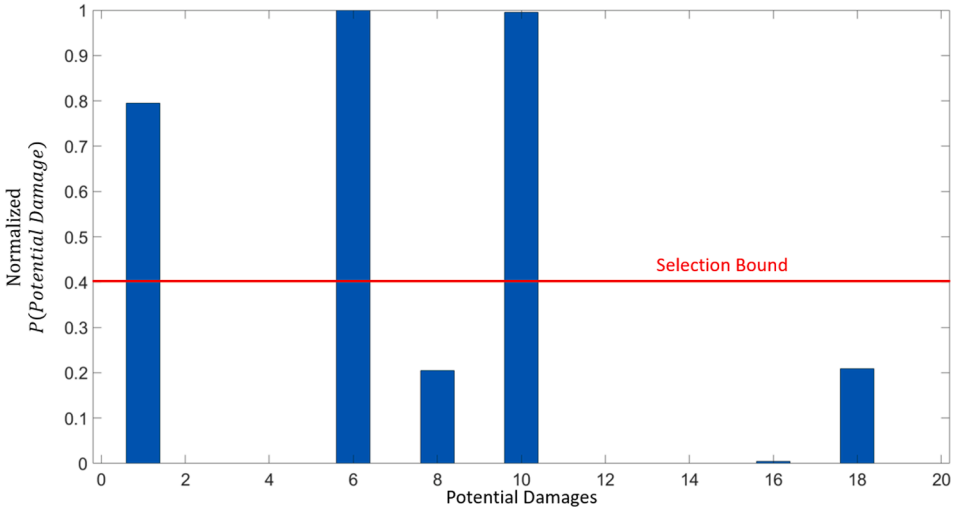

Fig. 5. Example of prediction screen selecting the most likely potential damages.

Fig. 6. A) downstream and b) upper views of Paraiso Bridge.

probability of a potential damage z, as shown in Equation (7):

$$P(PotentialDamage(z)) = \sum_{i=1}^{i=n} \boldsymbol{Q}_{(i,z)} * \frac{(1 - \boldsymbol{res}_i) * 10^K}{n} \qquad (7)$$
$$1 \leq z \leq \lambda$$

The probability of each potential damage is further normalized between 0 and 1 with respect to the maximum and minimum values obtained from Equation (7). Finally, the "selection bound" threshold is defined experimentally to select the most likely potential damages. This parameter defines the minimum weighted probability of a potential damage so as to be considered probable in predicting the damage scenario. The selection bound should be optimized in the parameter settings of the algorithm setup for each case study. Here, this parameter was optimized together with the factor K using a genetic algorithm and the objective function given in Equation (10) to maximize the success rate and minimize the number of false positives. As an example, Fig. 5 shows the normalized probability of occurrence of the different potential damages in a damage prediction scenario. Potential damages 1, 6, and 10 are selected as the most likely because they exceed the selection bound (0.4) obtained in Section 5.5, while potential damages 8, 16, and 18 are discarded.

3. Case study

3.1. Description of the bridge

The methodology was validated in a bridge over the Umia river in Vilagarcía de Arousa, west of the Galicia region, Spain. The bridge was constructed in 1897 by the English company Joseph Westwood & Co. It belonged to the railway route of Pontevedra-Vilagarcía de Arousa and was in service until 2008. In 2020 it was rehabilitated, and now it belongs to a pedestrian route, open to pedestrians and cyclists. The downstream and upper views of the bridge are shown in Fig. 6.

The structure is made of riveted steel with a total length of 15.6 m and a width of 5.8 m, supported by two masonry abutments. All steel members are manufactured with riveted steel plates and L-shaped profiles. The structural part of the bridge comprises two main girders with a high of 1.57 m and a width of 0.38 m joined by four cross-girders. The main girders are laterally stiffened using twenty-six web stiffeners and

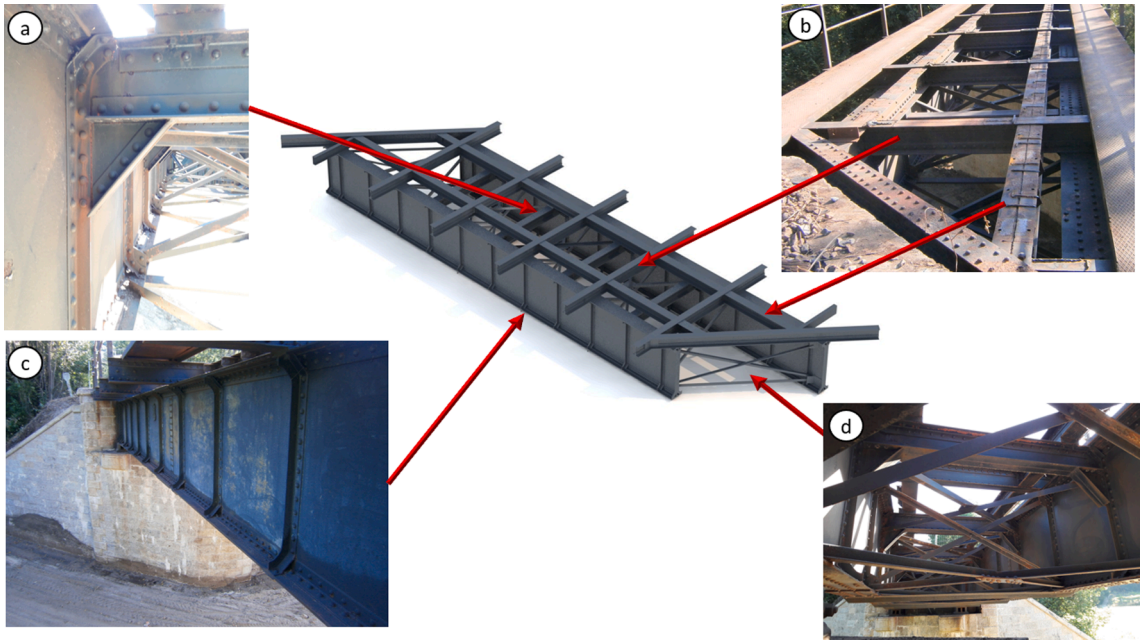

Fig. 7. Details of main elements of the bridge: a) Cross-girder b) Upper frame c) Main girder and web stiffeners d) L-shaped bracings.

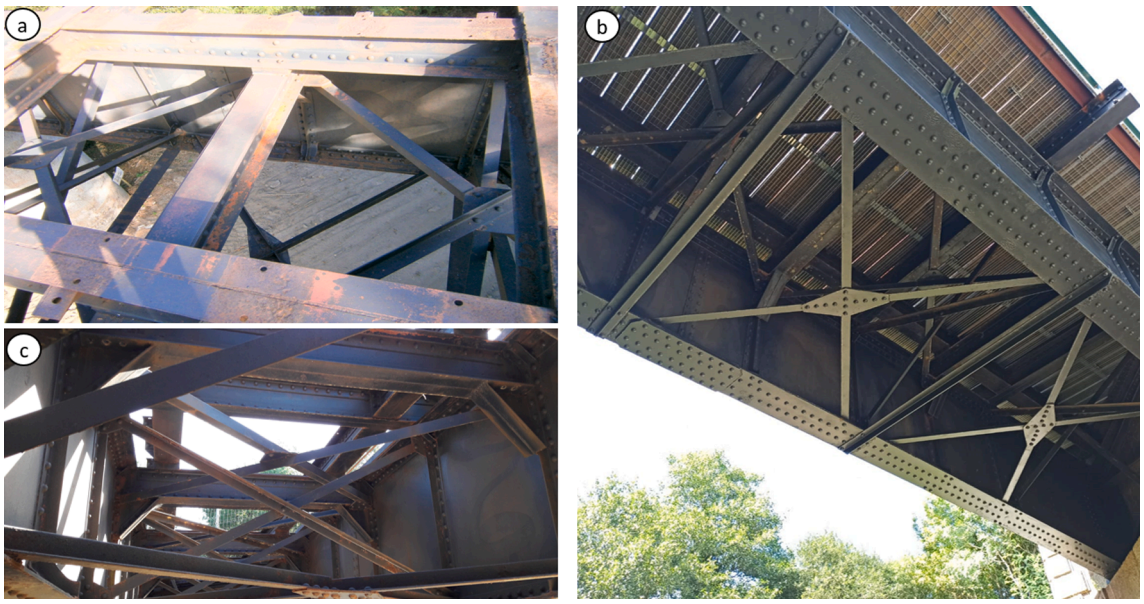

Fig. 8. Detail of the bracing systems: a) Upper bracings b) Lower bracings c) Middle bracings.

Fig. 9. Details of the corrosion state in two of the girder-bracings connections.

thirty-one L-shaped bracings. A frame consisting of two longitudinal and seven transverse beams rests over the main and cross-girders to distribute the loads. This frame and the remaining elements are shown in Fig. 7 and Fig. 8.

3.2. Experimental campaign

An extensive experimental campaign was deployed to obtain detailed information about the current condition state of the bridge. The campaign was divided into three main steps: I) visual inspection and on-site measuring to obtain the geometrical properties of the bridge and analyze its overall corrosion status; II) a terrestrial laser scanning (TLS) survey to obtain an accurate and detailed 3D geometrical model of the structure; III) an ambient vibration test (AVT) for characterizing the dynamic response of the bridge through the modal properties that will then be used in the calibration and damage prediction processes.

3.2.1. Visual inspection and on-site measuring

An in-depth visual inspection was carried out to obtain better knowledge about the corrosion status of the bridge. The inspection was

Table 1
Measurements of each member of the bridge. Steel plates dimensions are represented as width * thickness, while L-shaped profiles are represented as width1* width 2* thickness.

Element	Web (mm)	Flange (mm)	L-type profile (mm)
Main girders	1570*10	380*12	100*100*12
Cross-girders	290*10	210*(11 or 22)	90*90*10
Stringers of the upper frame	270*11	–	231*90*10
Transverse beams of the upper frame	310*10	–	190*90*13
Upper bracings	–	–	75*75*10
Middle bracings	–	–	60*60*10
Lower bracings	–	–	75*75*10
Web stiffeners	1552*10	140*10	–

performed before the rehabilitation works that were executed in 2020. During these works, the rail track was removed and replaced by a wood deck (see Fig. 7 b)). Thus, all structural elements could be inspected in detail. Generally, the bridge presents a moderate corrosion status except for the girders-bracings connections, identified as the most damaged elements, see Fig. 9.

Once the visual inspection was completed, on-site measurements were performed using a digital gauge with a tolerance of ± 0.01 mm and a laser distance meter to obtain the width and thickness of the different steel plates. These measurements were then complemented with the ones obtained from the Terrestrial Laser Scanning (TLS) survey. The summary of the experimental measurements is given in Table 1.

3.2.2. *Terrestrial laser scanning survey*

A Terrestrial Laser Scanning (TLS) survey was performed to obtain an accurate 3D model of the structure. This digitalization process aims to complement the measurements obtained in the previous stage, obtaining geometrical features that could not be taken manually. The instrument used is a phase-shift terrestrial laser scanner, model FARO Focus 3D [37]. This scanner presents an operational measurement range between 0.6 and 120 m in normal illumination conditions and a nominal accuracy of ± 2 mm at 25 m. The field of view is 305° vertically and 360° horizontally, and its maximum angular resolution is 0.009°. A total of 11 scans, collected from different scanner stations, were needed to complete the 3D model of the structure, as depicted in Fig. 10 a). The final point cloud comprises a total of 5.4 million points.

3.2.3. *Ambient vibration test*

An Ambient Vibration Test (AVT) was performed in the last step of the experimental campaign. The test was performed to characterize the dynamic behavior of the bridge in terms of its modal properties (natural frequencies, mode shapes, and damping ratios). These parameters constitute the ground truth data for the subsequent model updating process.

The equipment comprised five uniaxial seismic accelerometers type 8340 with a sensitivity of 10 V/g and an acquisition module type 3050 with a frequency range of 0–51.2 KHz, from Brüel & Kjaer company [38]. L-shaped steel supports were designed and manufactured to fix the accelerometers to the structure with the help of magnetic anchors. A multi-setup test was performed to overall characterize the structure with the available equipment. Accordingly, a preliminary finite element (FE) model of the bridge was developed to determine the main conditions of the test. Thus, fulfilling the criteria established by Ventura in [39] and Rodrigues [40], an acquisition frequency of 256 Hz and an acquisition time of 15 min per setup were adopted. The sensors were placed over the upper flange of the girder adjacent to each transverse beam, as represented in Fig. 11. Two sensors were placed in each measurement point, one in the vertical direction (Z axis) and the other in the transversal direction (Y axis). Point 3 was employed as a reference to avoid stationary conditions, while the remaining positions were covered by the roving sensors in a total of 6 setups.

As a result, a total of five vibration modes were identified. The first, fourth, and fifth mode shapes are horizontal bending modes, the second is a vertical bending mode, and the third is a torsional mode shape; see Fig. 12. The associated natural frequencies are summarized in Table 2.

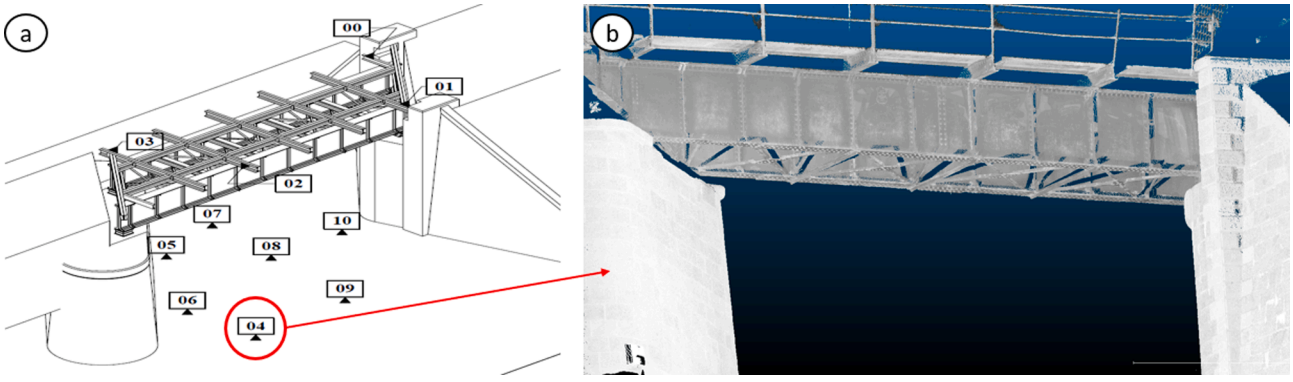

Fig. 10. A) outline of the laser scanning positions b) point cloud obtained from position 4.

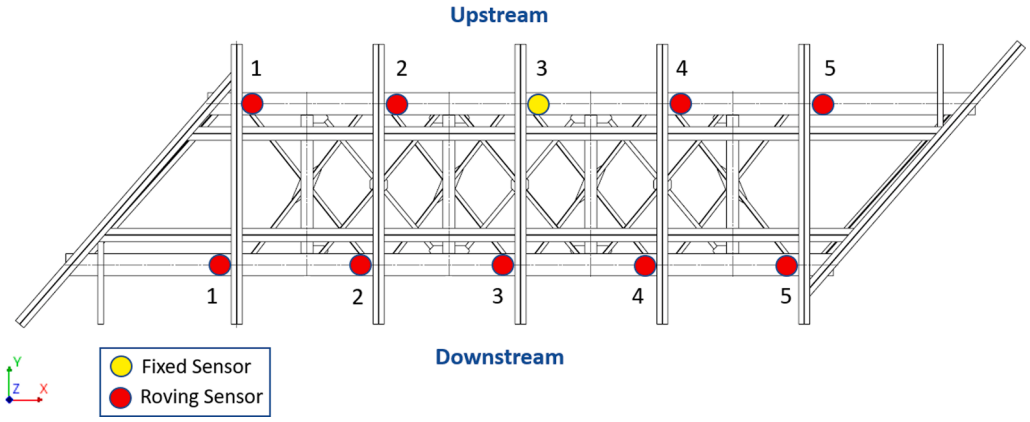

Fig. 11. Outline of the sensors location in the AVT.

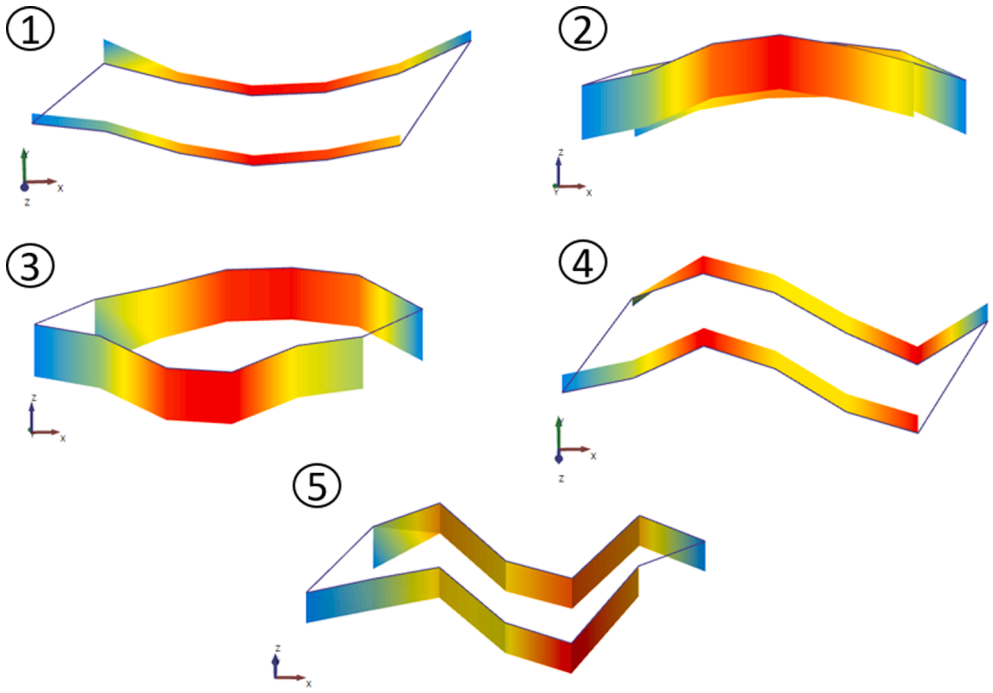

Fig. 12. Graphical representation of the five vibration modes obtained from the AVT.

Table 2
Summary of the natural frequencies obtained from the AVT.

Vibration mode	Frequency (Hz)
1	11.813
2	19.313
3	22.625
4	25.875
5	31.813

4. FEM-based modeling

A numerical model was developed using the Finite Element Method (FEM). The model was then calibrated using the data obtained from the AVT to reduce the uncertainty in the input parameters and, thus, obtain a FE model that accurately represents the actual bridge mechanical response.

4.1. FE model development

The FE model was built using the software Diana FEA [41]. The as-built geometrical model was created based on the point clouds and the on-site measurements, see Fig. 13. As for the mesh, four-node quadrilateral isoparametric shell elements with a global size of 0.05 m were adopted for almost all parts of the bridge except for the L-shaped bracings, which were modeled using two-node truss elements. The FE model was then further refined by adding interface elements in the supports of the bridge to represent possible aging effects affecting their stiffness. Moreover, the upper frame was substituted by equivalent point masses.

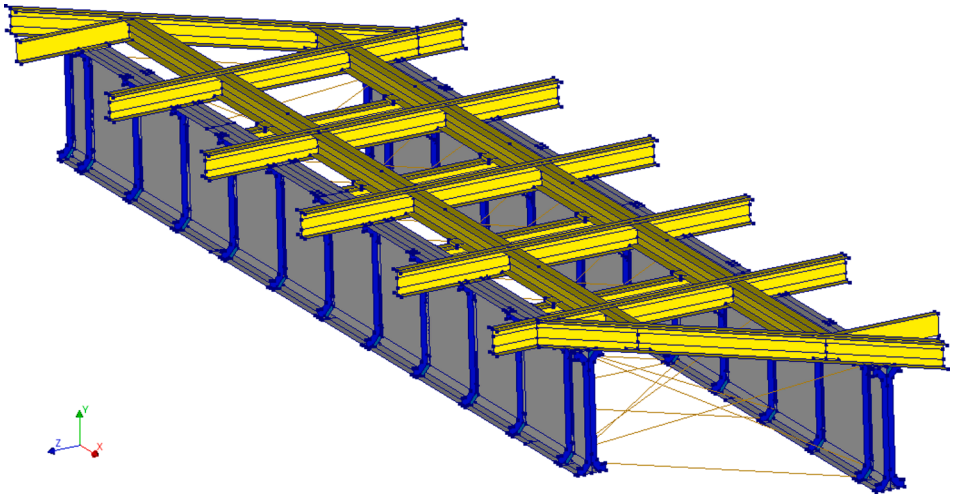

Fig. 13. Geometrical representation of the FE model of the bridge.

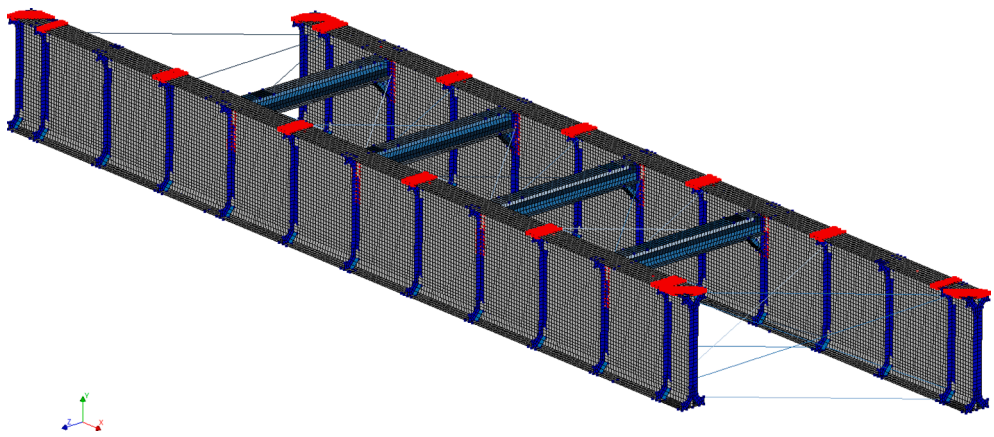

Fig. 14. Finite element mesh of the numerical model, with the point masses of the upper frame (highlighted in red). (For interpretation of the references to colour in this figure legend, the reader is referred to the web version of this article.)

Table 3
Parameters considered in the model updating process and their variation range.

ID	Type	Variable	Range Min	Max
V1	Steel material	Young's modulus (GPa)	170	232
V2		Density (Kg/m^3)	7615	8085
V3	Thickness reduction of bridge component cross-sections	Main girders (mm)	0	2
V4		Cross-girders (mm)	0	2
V5		Web stiffeners (mm)	0	2
V6		Upper bracings (mm)	0	2
V7		Middle bracings (mm)	0	2
V8		Lower bracings (mm)	0	2
V9	Stiffness of the support interfaces	K_{n1}(N/m^3)	1.00E + 09	1.00E + 10
V10		K_{t1}(N/m^3)	1.00E + 09	1.00E + 10
V11		K_{n2}(N/m^3)	1.00E + 09	1.00E + 10
V12		K_{t2}(N/m^3)	1.00E + 09	1.00E + 10

This was motivated by the fact that the frame is not rigidly connected to the main girders, thus being the stiffness contribution negligible. The final mesh and mass points of the upper frame are represented in Fig. 14.

4.2. FE model updating

Once the numerical model was developed, an updating process was carried out to reduce the input uncertainties and thus ensure the accuracy of the output results provided by the FE model. The uncertain model inputs can be divided into three main groups: I) material variables, II) geometrical variables, and III) supports stiffness variables.

- As for the material variables, the Young's modulus and the density of the steel were considered, while the Poison's ratio was fixed at 0.3. The density lower and upper bounds were established following the JCSS probabilistic model code [42], assuming a normal distribution with a mean of 7850 Kg/m^3, a Coefficient of Variation (CoV) of 1.0 %, and using the three-sigma rule of thumb that is equivalent to a confidence interval of 99.7% to determine the bounds of the interval. The variation range of the Young's modulus was chosen using the limits values corresponding to a confidence interval of 99.7%, as proposed in [43,44], being the values extracted from a lognormal distribution with a mean of 200 N/mm^2 and a CoV (Coefficient of Variation) of 5% [45].

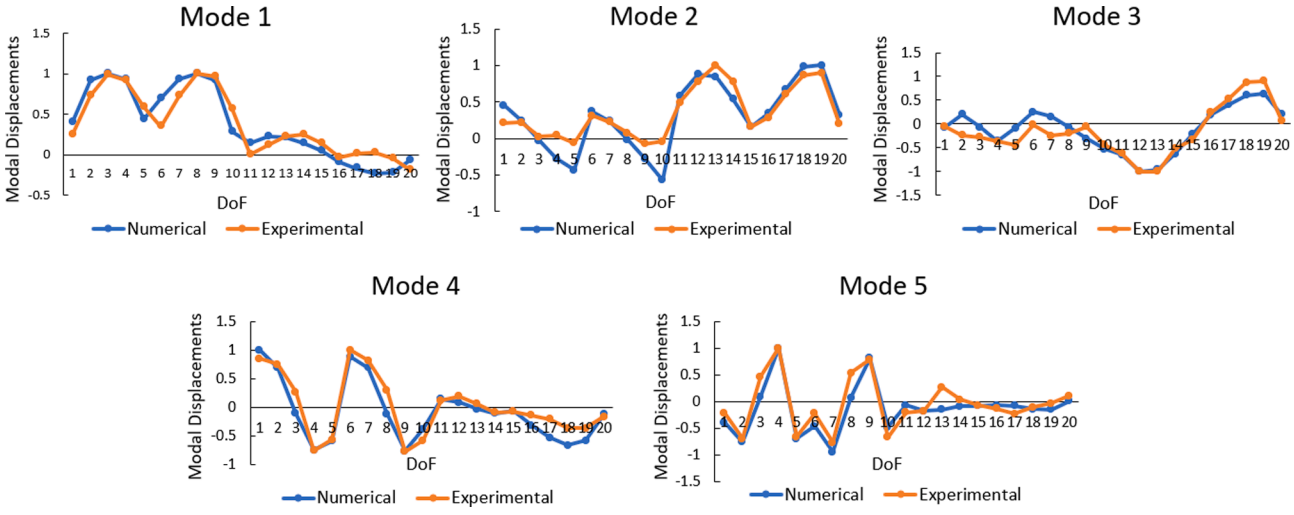

Fig. 15. Comparison between experimental and updated FE model modal displacements.

Table 4
Modal properties after FE model updating.

Mode	Experimental Frequency	Numerical Frequency	Error (%)	MAC
1	11.81	11.90	0.76%	0.96
2	19.31	19.36	0.26%	0.93
3	22.63	22.64	0.04%	0.91
4	25.88	25.91	0.12%	0.94
5	31.81	31.84	0.09%	0.91

Table 5
Updated parameter values obtained from the optimization process.

ID	Variable	Updated Value
V1	Young's modulus (GPa)	198.396
V2	Density (Kg/m^3)	7754.59
V3	Thickness reduction of main girders (mm)	0.222
V4	Thickness reduction of cross-girders (mm)	1.014
V5	Thickness reduction of web stiffeners (mm)	1.140
V6	Thickness reduction of upper bracings (mm)	1.190
V7	Thickness reduction of middle bracings (mm)	0.426
V8	Thickness reduction of lower bracings (mm)	1.914
V9	K_{n1}(N/m^3)	8.51E + 09
V10	K_{t1}(N/m^3)	4.20E + 09
V11	K_{n2}(N/m^3)	9.29E + 09
V12	K_{t2}(N/m^3)	4.95E + 09

- The geometrical variables were established for each steel member type. A total of six variables related to the cross-section thicknesses were considered, being the lower bound defined as the average experimental value obtained from the on-site measurements and the upper bound the average experimental measurements minus the maximum theoretical thickness reduction estimated from the current European standards of corrosion in metals [46,47]. Accordingly, a C4 corrosion category was chosen due to the localization of the bridge, which entails a maximum theoretical thickness reduction of 2.0 mm.
- Interface elements were introduced to model the normal (K_n) and tangential stiffness (K_t) of the right (K_{n1}, K_{t1}) and left supports (K_{n2}, K_{t2}). The range of variation was determined numerically from an extensive parametric analysis and considering the results obtained in the ambient vibration test (AVT). Thus, the bounds were restricted to the region that produces a minimum error between the FE model responses and the modal properties obtained from the AVT.

Table 3 summarizes the uncertain model inputs considered in the updating process and their variation range.

The FE model updating process was performed through the minimization of the following objective (error) function [48]:

$$\pi = W_{\mathscr{F}} \sum_{i=1}^{m} \left(\frac{\mathscr{F}_i^{num} - \mathscr{F}_i^{exp}}{\mathscr{F}_i^{exp}} \right)^2 + W_{MAC} \sum_{i=1}^{m} (1 - MAC_i)^2 \quad (8)$$

where $\mathscr{F}_i^{num}$ and $\mathscr{F}_i^{exp}$ are the numerical and experimental frequencies of each vibration mode, and MAC_i is the corresponding Modal Assurance Criterion between numerical and experimental modal displacements. Finally, $W_{\mathscr{F}}$ and $W_{MAC}$are the weighting factors of the frequency and MAC error terms, respectively. Weights of 0.5 were used for both factors to balance the contribution of both residual terms equally.

A gradient-based optimization method was adopted, namely the *lsqnonlin* function available in the MATLAB optimization toolbox [49]. This method was chosen due to the good balance between accuracy and computational cost, as it has been shown in previous similar studies [50–53]. Since this is a local optimization algorithm, a total of 50 samples were generated using the space-filling Latin Hypercube Sampling (LHS) technique [54] with the variation ranges defined in Table 3 to select suitable starting points that successfully cover all the search space. A high agreement between the numerical and experimental results was obtained, as shown in Fig. 15, where experimental and numerical modal displacements are graphically represented. As for the natural frequencies, an average relative error of 0.18% was obtained, which entails a noticeable agreement between both results. The error between the numerical and experimental frequencies and the MAC ratios of the calibrated FE model are summarized in Table 4. Finally, the updated values for the model parameters are given in Table 5.

5. Results

Once the previous steps were addressed, the validation through a real case study was carried out. First, the different potential damages were designed to represent all the damage possibilities of the structure. Then the initial assumptions were verified aiming to achieve realistic results and ensure their robustness. After these verifications, a two-stage optimization was performed to obtain the value of the different setting parameters of the methodology that maximize the accuracy of the results for the particular case study. Finally, the success and the false positives rate obtained for the optimized settings of the algorithm are discussed.

5.1. Potential damages

A total of nineteen potential damages were designed and simulated using the calibrated FE model. Sixteen potential damages simulate the loss of each pair of bracings. These damages were designed as local failures because the connections with the girders are the most damaged parts due to the corrosion pitting, as observed during the in-situ inspection. Herein, intermediate damage states prior to local collapses were not modeled due to the almost imperceptible changes induced in the modal parameters of the structure, which poses a challenge to their accurate identification. However, in other case studies, these intermediate damage states should be analyzed to evaluate the possibility of their implementation together with appropriate means of numerical modeling. In this sense, monitoring systems such as those described in [55,56] might also be adopted, thus providing valuable information for local damage detection and monitoring. Out of the sixteen damages related to local collapses, two are related to the bracings of the bridge ends (1–2), three are related to the upper bracings (3–5), four to the lower bracings (6–9), and the remaining seven damages are related to the bracings of the inner part of the bridge (10–16); see Table 6.

To cover all the damage possibilities, three more damages related to the corrosion in the main girders (17), the cross-girders (18), and the girders' web stiffeners (19) were considered. These damages represent a uniform corrosion situation, which together with the previous local damages, provide the necessary flexibility for the representation of the actual failure mechanism of the structure. Thus, following this approach, there may be situations in which the structure presents combinations of global (uniform) corrosion in conjunction with localized corrosion that would induce local failures. These damages were simulated as a net cross-section reduction. The amount of thickness reduction was set according to different factors. Initially, it was calculated following the standards [46,47] for a period of 10 years and assuming a C4 exposure category. Accordingly, a thickness reduction of 0.267 mm was obtained, equivalent to variations in the nominal cross-section dimensions between 2.05% and 3.33%, depending on the profile type. These thickness variations are of very low magnitude; hence, they do not cause appreciable variations in the modal properties of the structure besides being practically imperceptible to the eyes of an inspector. For this reason, it was decided to increase its value to 1.0 mm. This represents variations in the nominal cross-section dimensions that vary between 7.7% and 12.5%, which can be appreciated both in the dynamic response of the structure and by the human eye. It should be noted, however, that this value should be set according to the case study as the structure conditions may vary considerably. Briefly, using damage scenarios based on global (uniform) corrosion and local failures, such as the loss of bracings, provides sufficient flexibility to reasonably

Table 6
Modal properties values for the considered potential damage scenarios.

Potential Damages		F1	F2	F3	F4	F5	MAC1	MAC2	MAC3	MAC4	MAC5
0	FE Model	11.91	19.27	22.66	25.89	31.84	0.960	0.932	0.914	0.937	0.911
1	Bracings E1	11.78	19.25	22.17	25.69	31.81	0.959	0.927	0.899	0.913	0.909
2	Bracings E2	11.82	19.26	22.63	25.85	31.84	0.957	0.93	0.909	0.933	0.901
3	Bracings U1	11.55	18.95	22.67	24.23	31.43	0.968	0.915	0.915	0.835	0.885
4	Bracings U2	11.91	18.36	22.99	22.07	30.25	0.956	0.798	0.826	0.669	0.777
5	Bracings U3	11.24	18.95	22.66	24.79	31.52	0.944	0.886	0.909	0.914	0.883
6	Bracings L1	10.69	18.93	20.44	25.73	31.09	0.947	0.775	0.828	0.925	0.921
7	Bracings L2	11.88	19.20	22.42	24.80	31.73	0.962	0.930	0.937	0.935	0.919
8	Bracings L3	11.74	19.23	22.41	25.58	31.73	0.957	0.941	0.888	0.941	0.917
9	Bracings L4	10.17	19.22	22.09	25.09	31.07	0.966	0.939	0.965	0.931	0.792
10	Bracings M1	11.00	20.03	22.94	27.37	30.96	0.935	0.959	0.916	0.954	0.896
11	Bracings M2	11.08	19.13	21.28	23.68	31.74	0.926	0.845	0.645	0.623	0.706
12	Bracings M3	11.54	19.28	22.37	25.30	30.69	0.947	0.932	0.839	0.938	0.893
13	Bracings M4	11.81	19.28	22.60	25.88	31.84	0.961	0.932	0.913	0.930	0.911
14	Bracings M5	11.41	19.27	22.61	25.00	30.45	0.964	0.932	0.875	0.911	0.735
15	Bracings M6	10.76	19.19	23.50	22.11	31.73	0.973	0.904	0.687	0.655	0.876
16	Bracings M7	10.68	20.20	22.91	26.40	31.00	0.971	0.911	0.905	0.823	0.647
17	Main girder	11.90	18.87	22.43	25.71	31.33	0.958	0.939	0.916	0.939	0.893
18	Cross-girder	11.95	19.33	22.69	25.95	31.88	0.960	0.932	0.915	0.936	0.909
19	Web stiffeners	11.88	19.33	22.73	25.83	31.43	0.960	0.930	0.909	0.932	0.903

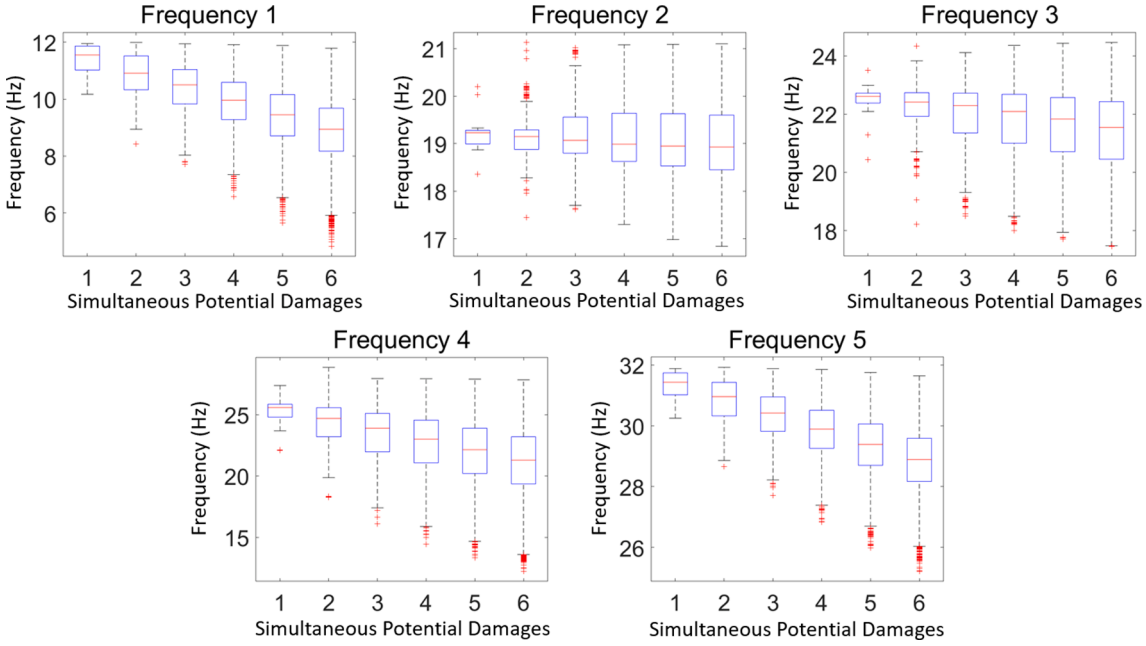

Fig. 16. Box and whisker plot of the natural frequencies (Y-axis) regarding the number of potential damages simultaneously applied (X-axis).

represent the corrosion effects on the structure.

Table 6 shows the modal properties obtained for each potential damage scenario. These nineteen damages cover all possible local failures except for the loss of stiffness at the supports, which were not considered because they are not easily quantifiable and out of the scope of this work. The loss of stiffness in the bridge supports or scouring are very complex problems that typically require a dedicated study [57,58]. Nevertheless, in this sense, it is worth mentioning that the algorithm developed also includes a warning when changes in the modal properties are detected, but they are not identified with the designed damages. Finally, the case 0 (the updated FE model without any damage) is also considered in the decision tree algorithm. If the code only selects this potential damage, a warning message is displayed, indicating that the algorithm could not detect any damage.

Moreover, the different combinations of potential damage were analyzed, contemplating from one to six potential damages simultaneously applied to obtain reference values that facilitate the evaluation of the bridge condition state. No more than six potential damages were considered since this would be an atypical situation within a routine inspection that probably has already triggered the bridge collapse. Thus, after performing all the damage combinations (43795 combinations), Box and Whisker plots were generated, showing the main statistical parameters of the modal responses. In these plots, the blue square indicates the values of the 75th and 25th percentiles; inside the square is the median value represented as a red horizontal line; outside the square, the maximum and minimum values are represented by black horizontal lines, and finally, outliers or atypical values are represented with a red asterisk. Accordingly, Fig. 16 and Fig. 17 show the Box and Whisker plots for the natural frequencies and MAC ratios, respectively. Based on them, the inspector can visually compare future dynamic

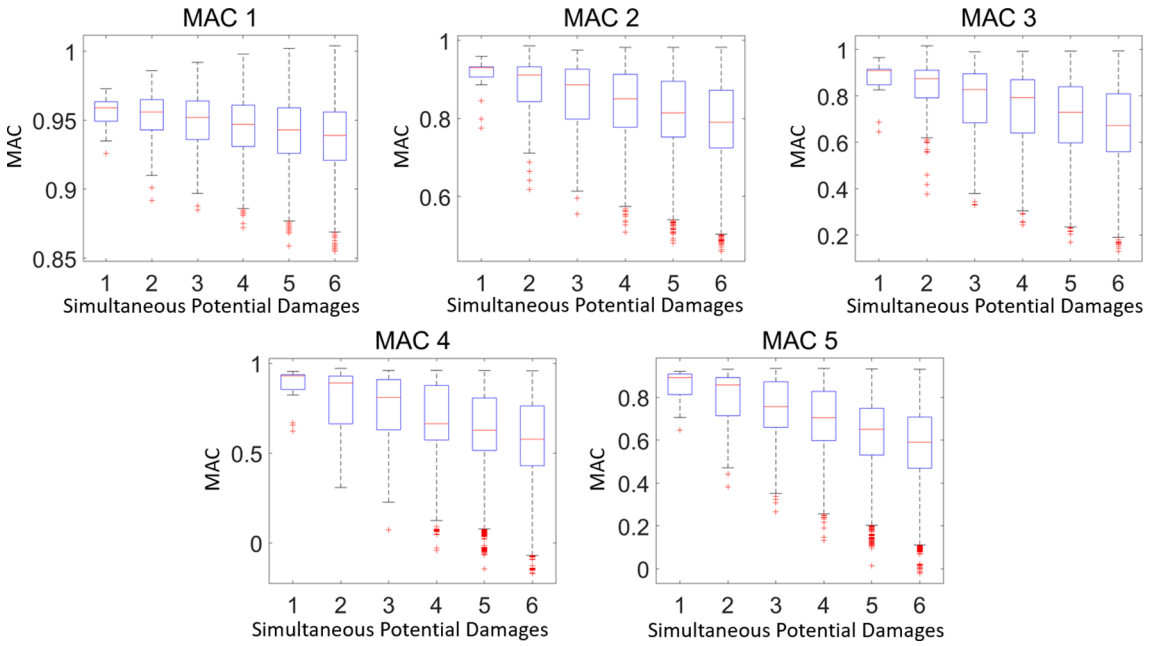

Fig. 17. Box and whisker plot of the MAC ratios (Y-axis) regarding the number of potential damages simultaneously applied (X-axis).

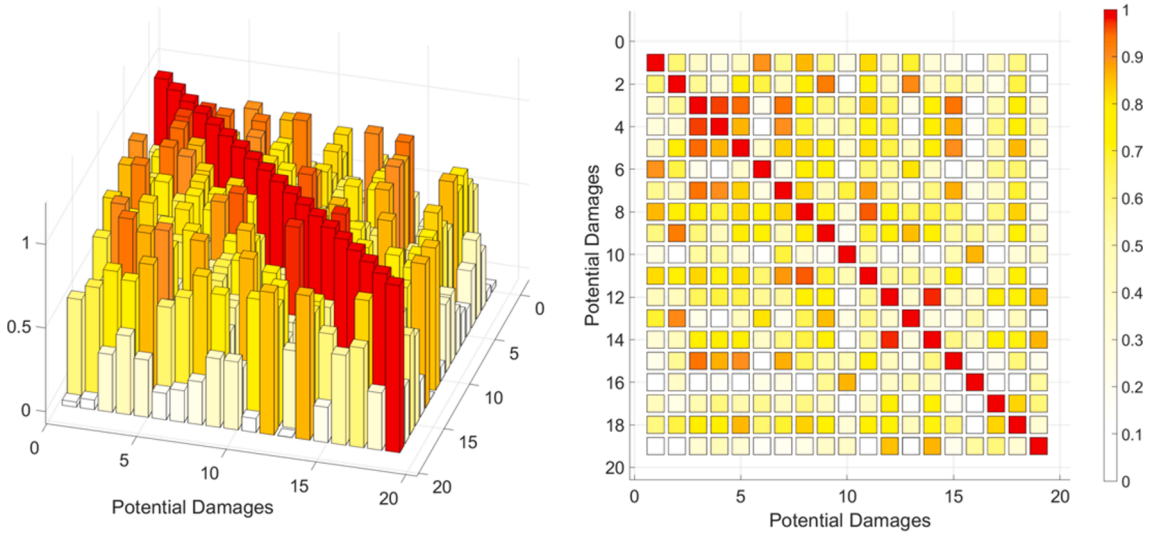

Fig. 18. MAC value among the modal properties changes from the different potential damages.

monitoring results with the modal parameters obtained from various simultaneously applied damages. This allows for establishing a reference of how critical the situation is.

5.2. Hypothesis of potential damages differentiation

Once the potential damages were designed, they were further analyzed to check how they affected the different modal properties. The higher the modal properties changes provoked by the potential damages, the greater success the algorithm will achieve in identifying them. Each potential damage was simulated to obtain the corresponding vector that clusters the modal properties changes (frequencies and MACs of the five vibration modes). Subsequently, the MAC of the different vectors was computed to check the similarity among the different effects of the damages. As a result, a graphical representation of the MAC values among all the damages effects was obtained. As depicted in Fig. 18, all the damages present significant discrepancies except for damages 3 and 12, which present high similarity with 4 and 14, respectively. Nonetheless, despite the high MAC values, the induced change in the modal properties is different. Thus, it can be concluded that the potential damages were designed in a way that they can be differentiable by the algorithm.

5.3. Hypothesis of cumulative damage

Before validating the methodology in a case study, the hypothesis of superposition of damages was evaluated. This analyzes whether the effect of various simultaneous potential damages can be quantified as the sum of the effects caused by each potential damage individually. It also assesses the error as a function of the number of simultaneous damages. In this way, the numerical simulation of the FE model at each node of the tree structure can be avoided, preventing the methodology from becoming a very expensive computational process (more than 500.000 possible damage combinations). An alternative approach would be

Table 7
Average relative error when comparing the effect of various potential damages evaluated directly with the calibrated FE model and the sum of the individual effects of each potential damage (superposition).

Average relative error Output\Potential damages	2	3	4	5	6
Frequency	0.06%	0.35%	0.44%	0.85%	0.86%
MAC	0.00%	0.89%	1.94%	3.21%	4.70%
Total	0.03%	0.62%	1.19%	2.03%	2.78%

building surrogate models to approximate the FE model responses for the different damage combinations. However, this is not a trivial task since accumulating multiple damages in the same scenario is a multi-model problem with complex non-linear relations between input (potential damages simultaneously applied) and output (modal properties variation) data that is not easily mappable.

Since the methodology focuses on early detection and localization of damage as a support tool in bridge inspections, priority has been given to detecting slight to moderate damage states produced by a limited accumulation of damages. Nonetheless, a scenario with several damages would have considerable changes in the modal properties so that even if not correctly predicted by the algorithm, a warning would be triggered advising of the anomaly that would serve to alert the inspector that structural safety may be being compromised and that a thorough inspection is necessary. Therefore, the prediction of severe damage states where nonlinearities are high is beyond the scope of the study and is considered a matter of further development. Accordingly, validation for a limited number of damage scenarios was performed in the present work.

To quantify the nonlinearity of the effects in the simultaneous application of damages, five datasets of 500 damages scenarios each were simulated, where two to six potential damages were applied simultaneously. The datasets were created using the LHS technique to explore the whole combination of damages with a minimum number of samples. Subsequently, the differences obtained between the direct evaluation of the FE model and the sum of the effects of each damage applied individually (superposition) were quantified. The average relative errors obtained are summarized in Table 7. As expected, the error increases with the number of damages applied simultaneously.

To establish a threshold value for the maximum admissible additivity error, the relative variations of the modal properties (ΔMP) for the different damage combinations with respect to the baseline calibrated FE model were calculated, as shown in Equation (9).

$$\Delta MP = \frac{\sum_{j=1}^{n} \frac{\sum_{i=1}^{m} \left| \frac{\mathscr{F}_{(j,i)}^{PD} - \mathscr{F}_{(i)}^{CAL}}{\mathscr{F}_{(i)}^{CAL}} \right| + \sum_{i=1}^{m} \left| \frac{MAC_{(j,i)}^{PD} - MAC_{(i)}^{CAL}}{MAC_{(i)}^{CAL}} \right|}{2*m}}{n} \tag{9}$$

where n is the number of potential damages (Table 6), m is the number of vibration modes, $\mathscr{F}_{(j,i)}^{PD}$ and $MAC_{(i)}^{PD}$ are the natural frequency and MAC ratio of vibration mode i and potential damage j, and $\mathscr{F}_{(i)}^{CAL}$ and $MAC_{(i)}^{CAL}$ the natural frequency and MAC ratio of vibration mode i for the calibrated FE model.

After performing the calculation, a ΔMP of 2.98% was obtained. Thus, in order to not exceed this value, it was decided to implement and validate the methodology with up to four potential damages simultaneously applied. In this regard, it must be noted that for real-world applications, scenarios consisting of four damages simultaneously applied could seriously compromise the structural integrity, even possibly leading to the structure collapse.

5.4. Environmental conditions and number of initial nodes

This section determines the optimal number of initial nodes to model the environmental conditions. Due to the geographical characteristics of the structure location, the presence of wind is of limited influence. Therefore, the distributed loads that would simulate its effect have not been considered. On the contrary, the bridge location is susceptible to significant changes in temperature and humidity, with temperatures reaching 35 °C in summer and negative values in winter. Therefore, to model the effects of temperature, a range of variation of 50 °C was considered, translating into an equivalent Young's modulus variation of 2.16 GPa according to Equation (3). Accordingly, the calibrated FE model was used to quantify the corresponding change in modal properties. As shown in Table 8, temperature variations induce changes in the natural frequencies up to 0.13 Hz while having little effect on the modal displacements.

In addition to temperature, other sources of uncertainty must be considered to ensure the robustness of the methodology. In the absence of wind, the remaining factors have a global effect on the structure; therefore, their effects can be modeled as stiffness variations. For this reason, they were also modeled by a Young's modulus variation using a safety coefficient (SC). The Young's modulus variation is introduced as Gaussian noise. To generate the Gaussian noise, a Normal distribution for the Young's modulus with a mean of 198.4 GPa (the calibrated value of the FE model) was assumed. According to the three-sigma rule of thumb, the standard deviation (σ) was calculated such that 99.7% of the population values were within the E-modulus variation range obtained for environmental conditions of ± ΔT*SC. Therefore, considering increments and decrements of 50° and a SC of 5.0, a standard deviation of 3.6 GPa was derived. This distribution yields samples with Young's modulus values from 187.6 to 209.2 GPa for 99.7% of the population values. This range of variation induces changes in modal properties that were simulated with the calibrated FE model and are summarized in Table 9.

As shown in Table 9, a SC of 5.0 induces variations in natural frequencies ranging from 0.52 to 1.32 Hz, with a relative variation between 4.0% and 5.0% with respect to the calibrated FE model. Case studies with similar approaches were reviewed in the existing literature, where they also used Gaussian noise to simulate environmental conditions and validate their methodologies. Most of these studies introduced a noise level (variation of modal parameters) of 1.0%, 2.0%, or 2.5% [59–62], while another study used a variation of up to 5.0% [63]. Here, the natural frequencies are higher than in the above studies, resulting in a more significant absolute frequency change. For this reason, the modal parameter variations obtained for a SC of 5.0 were considered acceptable to define the Gaussian noise used to validate the methodology and thus to quantify the environmental effects robustly.

Once the Gaussian noise used to model environmental effects was defined, it was also used to create the nodes of the first layer of the

Table 8
Changes originated in the modal properties for a ΔT = 50 °C.

ΔT = 50 °C (ΔE = 2.16 GPa) Vibration mode	ΔFrequency (Hz)	ΔMAC
Mode 1	0.060	0.000
Mode 2	0.100	0.001
Mode 3	0.120	0.001
Mode 4	0.120	0.003
Mode 5	0.130	0.001

Table 9
Changes in the modal properties for each vibration mode provoked by environmental conditions with an SC of 5.0.

Young Modulus (SC = 5) Vibration Mode	ΔFrequency (Hz)	ΔMAC	ΔFrequency (%)
Mode 1	0.520	0.001	4.37%
Mode 2	0.960	0.005	4.98%
Mode 3	1.080	0.006	4.77%
Mode 4	1.090	0.010	4.21%
Mode 5	1.320	0.007	4.15%

Table 10
R^2 and RMSE obtained for the surrogate model of each modal parameter.

Output	R^2	RMSE
Frequency 1	1.00	0.0038
Frequency 2	1.00	0.0041
Frequency 3	1.00	0.0036
Frequency 4	1.00	0.0030
Frequency 5	1.00	0.0030
MAC 1	0.96	0.0002
MAC 2	0.99	0.0003
MAC 3	1.00	0.0003
MAC 4	1.00	0.0003
MAC 5	1.00	0.0003

algorithm. Accordingly, the initial nodes will produce frequencies and MAC values corresponding to equidistant values of the Young's modulus over its range of variation. Therefore, surrogate models were used to compute these frequencies and MAC values and avoid the high computational cost associated with directly evaluating the FE model at each node. These approximation models were trained on a dataset of 1000 samples using the LHS technique [36]. The prediction accuracy was then quantified based on a 10-fold cross-validation procedure using two different metrics: the coefficient of determination (R^2) and the root mean square error (RMSE). In general, coefficients of determination above 0.90 provide acceptable accuracy for FE model responses, as stated in [64]. As shown in Table 10, the R^2 obtained for the ten outputs equals or exceeds 0.99, except for the first MAC (0.96). This is because the response is almost constant; however, it can be seen that it presents a lower RMSE value (0.0002). Therefore, it can be concluded that the surrogate models accurately replace the FE model with minimum computational cost.

Regarding the number of nodes of the first layer, a large number allows us to predict the most likely environmental conditions more precisely, but at the same time, it increases the computational cost critically. For this reason, a parametric analysis was performed to evaluate the success rate of the algorithm and the computational cost as a function of the number of initial nodes. The success rate is defined as the number of damages correctly predicted by the algorithm over the total number of damages that compose each damage scenario. Thus, the number of initial nodes was varied from 5 to 125 in steps of 5. A total of 25 datasets containing 500 damage scenarios (each with two to four potential damages simultaneously applied) were simulated for this comparison. The computational cost (time) and success rate were finally normalized between [0–1] to compare both factors properly. Fig. 19 shows the representation of both magnitudes for the different number of initial nodes. As can be observed, the increase in the computational cost follows a linear trend. However, the success rate increases asymptotically so that from 95 nodes, it remains almost constant. For this reason, the number of initial nodes was fixed at 100, looking for a balance between accuracy and computational cost.

5.5. Optimization of error ponderation and selection bound

Once the number of initial nodes was determined, the following parameters were adjusted to maximize the accuracy of the whole methodology: the number of paths (N), the error ponderation (k), and the selection bound.

First, several simulations were performed to determine the optimal value of N. The larger the value of this parameter, the more thoroughly all damage possibilities are explored to predict each damage scenario. This results in a deeper exploration of the different damage combinations but also a significant increase in computational cost due to the large number of evaluations required. In other case studies where the effects of the potential damages are similar, resorting to high N values may be necessary. However, for the bridge studied here, since the potential damages induce significant differences in the modal properties, as shown in Fig. 18, the algorithm already achieves reasonably good results by setting $N = 2$, thus implying a lower computational cost and a lower false positive rate.

Once the parameter N was determined, the error ponderation (k) and the selection bound were optimized. Since these parameters presented strong interaction effects, manual tuning was discarded. Thus, an optimization process using a genetic algorithm was performed to obtain the best combination of values that ensure a higher success rate. This methodology was chosen because it is a global optimizer that fully explores the search space. The problem was formulated as a discrete optimization in which the parameters were optimized with a resolution of 0.1, aiming to find a balance between accuracy and computational cost. The ranges of both parameters were obtained through a parametric analysis exploring the sensitive regions for each variable. For the error ponderation (k), a range of [1-10] was determined (see Table 11) since outside this range, the prediction results of the algorithm hardly showed any variation. As for the selection bound, a range of [0.1 to 0.9] was determined since the variable's influence was notably lower towards the

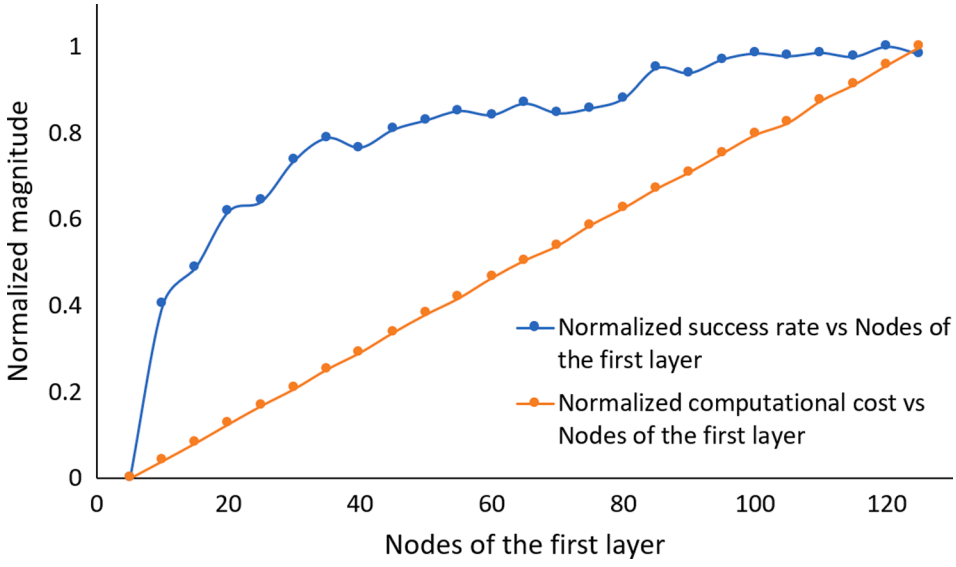

Fig. 19. Comparison of success rate (blue) and computational cost (orange), both normalized between [0–1] when estimating environmental conditions using a different number of initial nodes. (For interpretation of the references to colour in this figure legend, the reader is referred to the web version of this article.)

Table 11
Ranges of the setting parameters in the optimization process.

Parameter	Range	
	Min	Max
Error Ponderation (k)	1	10
Selection Bound	0.1	0.9

extremes of the search space.

Subsequently, the optimization process was carried out using as an objective a function that quantifies the average Success Rate (SR) and the number of False Positives (FP) for a dataset composed of 500 damage scenarios to be predicted. The SR was previously defined, while the FP is defined as the number of damages incorrectly selected by the algorithm that are not part of the scenario to be predicted. The objective function is defined in Equation (10):

$$f = W_{SR}*\frac{100 - SR}{100} + W_{FP}*FP \tag{10}$$

where W_{SR} and W_{FP} are weighting factors that were fixed at 1.0 and 0.05, respectively. These weights were selected after performing several simulations and evaluating both terms of the objective function. These weight values mean a 95 % success rate would result in the same error as one false positive. In this sense, it was considered that for the sake of structural safety, it would be critical that the algorithm identified as false positive an actual damage. The objective function was minimized using a genetic algorithm, where the initial population consisted of 100 individuals created using Latin Hypercube Sampling (LHS). The five individuals with the best fitness values were passed to the next generation (elitism). Regarding the new individuals, 70% were created using crossover, while 30% were created using mutation. The algorithm was run for 150 generations. The optimal values for the setting parameters were 8 for the error ponderation (k) and 0.4 for the selection bound. The response surface described by the results at each iteration of the optimization process is depicted in Fig. 20.

5.6. Validation results

After the setting parameters were optimized for the case study, a final validation was performed to obtain an average success and false positives rate. The false positives rate is defined as the number of damages incorrectly selected by the algorithm (false positives) over the sum of the number of false positives and the total number of damages not part of the scenario to be predicted (true negatives).

To perform the validation, 20.000 damage scenarios (each with one to four potential damages simultaneously applied) were simulated to test the decision tree algorithm. Thus, a random dataset composed of nineteen columns (one for each potential damage) was created, where each column was filled with ones and zeros depending on whether or not the damage was present. Then, for the potential damages simultaneously

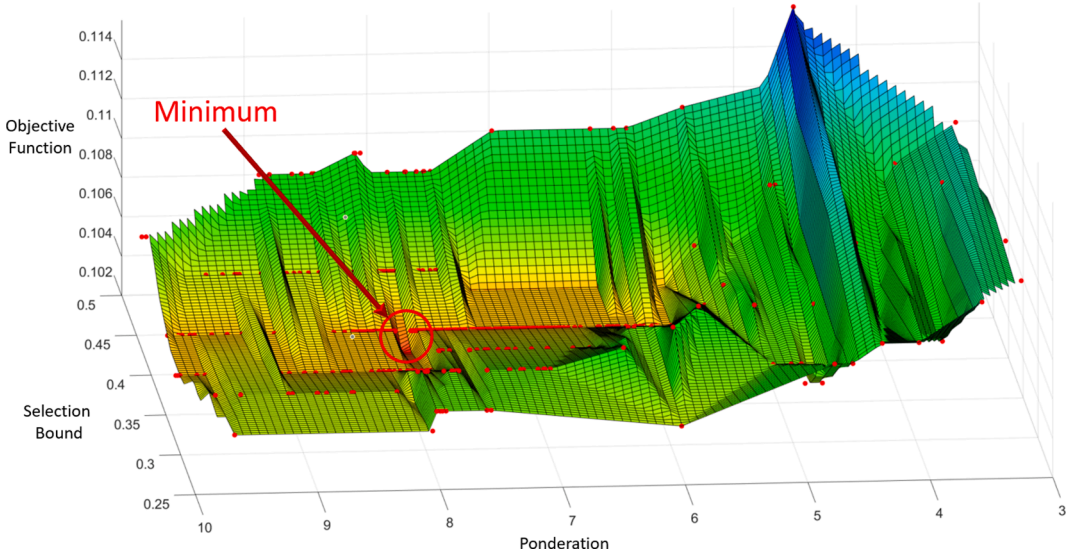

Fig. 20. Graphical representation of the objective function response surface obtained in the optimization process of the parameter settings of the developed decision tree algorithm.

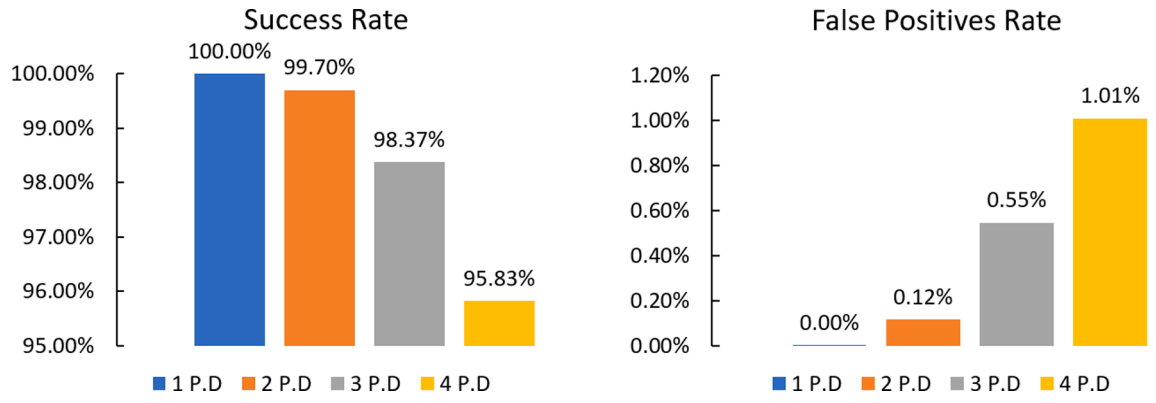

Fig. 21. Average success and false positives rate for different potential damages (P.D) simultaneously applied.

applied, the modal properties were computed using the updated FE model. Finally, Gaussian noise was applied, as explained in section 5.4. The success rate and the number of false positives were determined for each prediction.

Thus, an average success rate of 95.83% and an average false positive rate of 1.01% were obtained. Analyzing the results (see Fig. 21), a significant improvement can be observed when the maximum number of damages simultaneously applied decreases. In this sense, as the simultaneous damages increase, nonlinearities in the changes of the modal parameters are more significant, as discussed in section 5.3. The obtained results verify that the hypotheses were correctly validated and that the decision tree algorithm can provide robust and confident predictions.

6. Conclusions

A model-based decision tree algorithm was designed and implemented to predict damage in a riveted steel truss bridge. This algorithm is conceived to work as a cost-effective routine bridge inspector that detects and locates potential damages in the structure based on its actual modal properties.

To implement the algorithm in a real case study, it was necessary to carry out an experimental campaign in which multi-source data were collected. Additionally, a detailed FE model was developed to study how the different potential damages affected the dynamic response of the bridge. This numerical model was calibrated with vibration-based data to accurately reflect the actual mechanical response. Subsequently, the potential damages were designed, and the algorithm parameters were adjusted. For this purpose, a genetic algorithm was employed to optimize the most critical parameters. The methodology was validated with a total of 20,000 predictions in which Gaussian noise was introduced to simulate the environmental conditions. As a result, the algorithm delivered predictions with an average success rate of 95.83% and an average false positive rate of 1.01%.

The main advantage provided by this methodology is that it is a cost-effective solution that can detect local damages in structural components that are not easily accessible during routine bridge inspections. This way, the algorithm has great potential in terms of robustness, as it avoids human errors in diagnosing elements that are not visible to the inspectors. The work will contribute to setting a training dataset for future AI-based algorithms, such as deep learning models that can work as surrogate models so that the methodology can be easily transferred to other bridge typologies.

CRediT authorship contribution statement

B. Barros: Methodology, Software, Investigation, Writing – original draft. **B. Conde:** Conceptualization, Methodology, Investigation, Supervision, Writing – review & editing. **M. Cabaleiro:** Resources, Supervision. **B. Riveiro:** Funding acquisition, Supervision, Writing – review & editing.

Declaration of Competing Interest

The authors declare the following financial interests/personal relationships which may be considered as potential competing interests: [Belen Riveiro Rodriguez reports financial support was provided by the European Union's Horizon 2020 research and innovation program under grant agreement No. 958171. Belen Riveiro Rodriguez reports financial support was provided by 2021 Leonardo Grant for Researchers and Cultural Creators, BBVA Foundation. Brais Barros Gonzalez reports financial support was provided by Spanish Ministry of Science, Innovation, and Universities through the grant PRE2019-087331. Borja Conde Carnero reports financial support was provided by Spanish Ministry of Science, Innovation, and Universities through the human resources program "Jose Castillejo 2021" (Ref.: CAS21/00203)].

Data availability

The authors do not have permission to share data.

Acknowledgments

This project has received funding from the European Union's Horizon 2020 research and innovation program under grant agreement No. 958171.Work produced with the support of a 2021 Leonardo Grant for Researchers and Cultural Creators, BBVA Foundation. The BBVA Foundation takes no responsibility for the opinions, statements, and contents of this project, which are entirely the responsibility of its authors. The support of the Spanish Ministry of Science, Innovation, and Universities through the grant PRE2019-087331 is acknowledged. Work produced with the support of the Spanish Ministry of Universities through the human resources program "Jose Castillejo 2021" (Ref.: CAS21/00203).

References

[1] A. K. Funk, Transport Infrastructure Investments in Switzerland [Online]. Available EUROCONSTRUCT 2017. http://www.tecninvest.com/euroconstruct.html.
[2] "Report card for america's infraestructure," pp. 18–25, [Online]. Available: https://infrastructurereportcard.org/cat-item/bridges-infrastructure/.
[3] Casas JR. The bridges of the future or the future of bridges? Front Built Environ 2015;1(April):1–3. https://doi.org/10.3389/fbuil.2015.00003.
[4] Z. Fu, B. Ji, M. Cheng, and H. Maeno, "Statistical analysis of cause of bridge collapse in China," *Forensic Eng. 2012 Gatew. to a Better Tomorrow - Proc. 6th Congr. Forensic Eng.*, pp. 75–83, 2013, doi: 10.1061/9780784412640.009.
[5] Wardhana K, Hadipriono FC. Analysis of recent bridge failures in the United States. J Perform Constr Facil 2003;17(3):151–8. https://doi.org/10.1061/(ASCE)0887-3828(2003)17:.
[6] Sousa JJ, Bastos L. Multi-temporal SAR interferometry reveals acceleration of bridge sinking before collapse. Nat Hazards Earth Syst Sci 2013;13(3):659–67. https://doi.org/10.5194/nhess-13-659-2013.
[7] Cusumano N, Siemiatycki M, Vecchi V. The politicization of public–private partnerships following a mega-project disaster: the case of the Morandi Bridge Collapse. J Econ Policy Reform 2020;00(00):1–17. https://doi.org/10.1080/17487870.2020.1760101.
[8] "Un problema oculto en un viaducto de la A6 en la entrada a Galicia, posible causa de un colapso 'sin precedentes,'" *elDiario.es*.
[9] Tan JS, Elbaz K, Wang ZF, Shen JS, Chen J. Lessons learnt from bridge collapse: A view of sustainable management. Sustain 2020;12(3):1–16. https://doi.org/10.3390/su12031205.
[10] An Y, Chatzi E, Sim SH, Laflamme S, Blachowski B, Ou J. Recent progress and future trends on damage identification methods for bridge structures. Struct Control Heal Monit 2019;26(10):1–30. https://doi.org/10.1002/stc.2416.
[11] McCann DM, Forde MC. Review of NDT methods in the assessment of concrete and masonry structures. NDT E Int 2001;34(2):71–84. https://doi.org/10.1016/S0963-8695(00)00032-3.
[12] Tokognon CJA, Gao B, Tian GY, Yan Y. Structural Health Monitoring Framework Based on Internet of Things: A Survey. Proc. - 2016 3rd Int. Conf. Syst. Collab. SysCo 2016 2017;4(3):619–35. https://doi.org/10.1109/JIOT.2017.2664072.
[13] Oh BK, Park HS, Glisic B. Prediction of long-term strain in concrete structure using convolutional neural networks, air temperature and time stamp of measurements. Autom Constr 2021;126:103665. https://doi.org/10.1016/j.autcon.2021.103665.
[14] Du C, Dutta S, Kurup P, Yu T, Wang X. "A review of railway infrastructure monitoring using fiber optic sensors", *Sensors Actuators*. A Phys 2020;303:111728. https://doi.org/10.1016/j.sna.2019.111728.
[15] A. Moghadam, M. AlHamaydeh, and R. Sarlo, "Bridge-weigh-in-motion approach for simultaneous multiple vehicles on concrete-box-girder bridges," *Autom. Constr.*, vol. 137, no. October 2021, p. 104179, 2022, doi: 10.1016/j.autcon.2022.104179.
[16] M. A. Mendoza-Lugo and O. Morales-Nápoles, "Vehicular loads hazard mapping through a Bayesian Network in the State of Mexico," *Proc. 31st Eur. Saf. Reliab. Conf. ESREL 2021*, pp. 2510–2517, 2021, doi: 10.3850/978-981-18-2016-8_289-cd.
[17] M. A. Mendoza-Lugo, O. Morales-Nápoles, and D. J. Delgado-Hernández, "A Non-parametric Bayesian Network for multivariate probabilistic modelling of Weigh-in-Motion System Data," *Transp. Res. Interdiscip. Perspect.*, vol. 13, no. September 2021, p. 100552, 2022, doi: 10.1016/j.trip.2022.100552.
[18] Xu Y, Zhang J. UAV-based bridge geometric shape measurement using automatic bridge component detection and distributed multi-view reconstruction. Autom Constr 2022;140:104376. https://doi.org/10.1016/j.autcon.2022.104376.
[19] Chen S, Laefer DF, Mangina E, Zolanvari SMI, Byrne J. UAV Bridge Inspection through Evaluated 3D Reconstructions. J Bridg Eng 2019;24(4):1–15. https://doi.org/10.1061/(asce)be.1943-5592.0001343.
[20] B. Riveiro and M. Solla *Non-Destructive Techniques for the Evaluation of Structures and Infrastructure*; 2016. doi: 10.1201/b19024.
[21] Jang K, Jung H, An YK. Automated bridge crack evaluation through deep super resolution network-based hybrid image matching. Autom Constr 2022;137:104229. https://doi.org/10.1016/j.autcon.2022.104229.

[22] H. Salehi and R. Burgueño, "Emerging artificial intelligence methods in structural engineering," *Eng. Struct.*, vol. 171, no. September 2018, pp. 170–189, 2018, doi: 10.1016/j.engstruct.2018.05.084.
[23] Azimi M, Eslamlou AD, Pekcan G. Data-driven structural health monitoring and damage detection through deep learning. State-of the-art review 2020. https://doi.org/10.3390/s20102778.
[24] Doebling SW, Farrar CR, Prime MB. Summary Review of Vibration-Based Damage Identification Methods. Shock Vib Dig 1998;30(march):91–105. https://doi.org/10.1177/058310249803000201.
[25] Kong X, Cai CS, Hu J. The state-of-the-art on framework of vibration-based structural damage identification for decision making. Appl Sci 2017;7(5):pp. https://doi.org/10.3390/app7050497.
[26] Santos JP, Cremona C, Orcesi AD, Silveira P. Early Damage Detection Based on Pattern Recognition and Data Fusion. J Struct Eng 2017;143(2):1–11. https://doi.org/10.1061/(asce)st.1943-541x.0001643.
[27] K.B. Bharadwaj Prakash, and G.R. Kanagachidambaresa. Pattern Recognition and Machine Learning; 2021.
[28] Parisi F, Mangini AM, Fanti MP, Adam JM. Automated location of steel truss bridge damage using machine learning and raw strain sensor data. Autom Constr 2022; 138:104249. https://doi.org/10.1016/j.autcon.2022.104249.
[29] Lin F, Scherer RJ. Concrete bridge damage detection using parallel simulation. Autom Constr 2020;119:103283. https://doi.org/10.1016/j.autcon.2020.103283.
[30] Pastor M, Binda M, Harčarik T. Modal assurance criterion. Procedia Eng 2012;48: 543–8. https://doi.org/10.1016/j.proeng.2012.09.551.
[31] Luecke WE, et al. "Mechanical Properties of Structural Steels", *NIST NCSTAR 1–3D Fed* [Online].Available: Build Fire Saf Investig World Trade Cent Disaster 2005. https://www.nist.gov/publications/mechanical-properties-structural-steels-federal-building-and-fire-safety-investigation.
[32] Erazo K, Sen D, Nagarajaiah S, Sun L. Vibration-based structural health monitoring under changing environmental conditions using Kalman filtering. Mech Syst Signal Process 2019;117:1–15. https://doi.org/10.1016/j.ymssp.2018.07.041.
[33] Santner TJ, Williams BJ, Notz WI. The Design and Analysis of Computer Experiments. New York, NY: Springer; 2003.
[34] Sacks J, Welch WJ, Mitchell YJ, Wynn HP. Design and Analysis of Computer Experiments. Stat Sci 1989;4:409–35. https://doi.org/10.1214/ss/1177012413.
[35] C. Lataniotis, S. Marelli, and B. Sudret, "Kriging UqLab User Manual (Gaussian Process Modelling)," [Online]. Available: https://www.uqlab.com/user-manuals.
[36] McKay MD, Beckman RJ, Conover WJ. Comparison of three methods for selecting values of input variables in the analysis of output from a computer code. Technometrics 1979;21(2):239–45. https://doi.org/10.1080/00401706.1979.10489755.
[37] "Faro Focus 3 D (FARO Technologies Inc., Lake Mary, Florida, USA)." https://www.faro.com/.
[38] "BRÜEL & KJAER and HBK company." https://www.bksv.com/.
[39] Brincker R, Ventura CE. Introduction to operational modal analysis. John Wiley & Sons Ltd; 2015.
[40] J. Rodrigues, "Identificação Modal Estocástica: Métodos de Análise e Aplicações em Estruturas de Engenharia Civil," 2004.
[41] Computational Mechanics department of TNO Building and construction research institute, "DIANA FEA BV Documentation." Delt,The Netherlands, 2003, [Online]. Available: https://dianafea.com.
[42] JCSS, "Probabilistic Model Code - Part 2: Load Models," pp. 1–73, 2001.
[43] Bouzas O, Conde B, Cabaleiro M, Riveiro B. A holistic methodology for the non-destructive experimental characterization and reliability-based structural assessment of historical steel bridges. Eng Struct 2022;270:114867. https://doi.org/10.1016/j.engstruct.2022.114867.
[44] Barbato M, Gu Q, Conte JP. Probabilistic push-over analysis of structural and soil-structure systems. J. Struct. Eng. 2010:1330–41. https://doi.org/10.1061/(ASCE)ST.1943-541X.0000231.
[45] Park CB, Miller RD, Xia J. Multichannel analysis of surface waves. Geophysics 1999;64:800–8. https://doi.org/10.1190/1.1444590.
[46] *AENOR Part 1: Corrosion of metals and alloys - Corrosivity of atmospheres - Classification, determination and estimation (ISO 92232012)*.
[47] *AENOR Part 2: Corrosion of metals and alloys - Corrosivity of atmospheres - Guiding values for the corrosivity categories (ISO 9224:2012)*.
[48] Bautista-De Castro Á, Sánchez-Aparicio LJ, Ramos LF, Sena-Cruz J, González-Aguilera D. Integrating geomatic approaches, Operational Modal Analysis, advanced numerical and updating methods to evaluate the current safety conditions of the historical Bôco Bridge. Constr Build Mater 2018;158:961–84. https://doi.org/10.1016/j.conbuildmat.2017.10.084.
[49] Mathworks, "MathWorks. MatLab user manual,Least-Squares (Model Fitting) Algorithms." https://es.mathworks.com/help/optim/ug/least-squares-model-fitting-algorithms.html.
[50] R. Ferrari, D. Froio, E. Rizzi, C. Gentile, and E. N. Chatzi, "Model updating of a historic concrete bridge by sensitivity- and global optimization-based Latin Hypercube Sampling," *Eng. Struct.*, vol. 179, no. November 2018, pp. 139–160, 2019, doi: 10.1016/j.engstruct.2018.08.004.
[51] Bautista-De Castro Á, Sánchez-Aparicio LJ, Carrasco-García P, Ramos LF, González-Aguilera D. A multidisciplinary approach to calibrating advanced numerical simulations of masonry arch bridges. Mech Syst Signal Process 2019;129:337–65. https://doi.org/10.1016/j.ymssp.2019.04.043.
[52] Conde B, Ramos LF, Oliveira DV, Riveiro B, Solla M. Structural assessment of masonry arch bridges by combination of non-destructive testing techniques and three-dimensional numerical modelling: Application to Vilanova bridge. Eng Struct 2017;148:621–38. https://doi.org/10.1016/j.engstruct.2017.07.011.
[53] X. Dong and Y. Wang, "Finite Element Model Updating of a Steel Pedestrian Bridge Model," *Comput. Civ. Eng. 2019 Smart Cities, Sustain. Resil.*, pp. 397–404, 2019, doi: 10.1061/9780784482445.051.
[54] Lataniotis C, Marelli S, Sudret B. "UQLab user manual–The Input module", *Chair of Risk, Safety and Uncertainty Quantification* 2015;Report No. UQLab-V1:2–102 [Online].Available: https://www.uqlab.com/user-manuals.
[55] Marques F, Moutinho C, Magalhães F, Caetano E, Cunha Á. Analysis of dynamic and fatigue effects in an old metallic riveted bridge. J Constr Steel Res 2014;99: 85–101. https://doi.org/10.1016/j.jcsr.2014.04.010.
[56] V. Sangiorgio, A. Nettis, G. Uva, F. Pellegrino, H. Varum, and J. M. Adam, "Analytical fault tree and diagnostic aids for the preservation of historical steel truss bridges," *Eng. Fail. Anal.*, vol. 133, no. December 2021, p. 105996, 2022, doi: 10.1016/j.engfailanal.2021.105996.
[57] Chou JS, Pham AD. Hybrid computational model for predicting bridge scour depth near piers and abutments. Autom Constr 2014;48:88–96. https://doi.org/10.1016/j.autcon.2014.08.006.
[58] Chou JS, Nguyen NM. Scour depth prediction at bridge piers using metaheuristics-optimized stacking system. Autom. Constr. 2020;140:104297. https://doi.org/10.1016/j.autcon.2022.104297.
[59] Panigrahi SK, Chakraverty S, Mishra BK. Vibration based damage detection in a uniform strength beam using genetic algorithm. Meccanica 2009;44(6):697–710. https://doi.org/10.1007/s11012-009-9207-1.
[60] "Structural Damage Identification Using Response Surface-Based multi-objetive optimization.pdf.".
[61] Xia Y, Hao H. Statistical damage identification of structures with frequency changes. J Sound Vib 2003;263(4):853–70. https://doi.org/10.1016/S0022-460X(02)01077-5.
[62] Pathirage CSN, Li J, Li L, Hao H, Liu W, Ni P. Structural damage identification based on autoencoder neural networks and deep learning. Eng Struct 2018;172: 13–28. https://doi.org/10.1016/j.engstruct.2018.05.109.
[63] Ge M, Lui EM. Structural damage identification using system dynamic properties. Comput Struct 2005;83(27):2185–96. https://doi.org/10.1016/j.compstruc.2005.05.002.
[64] Jin SS, Jung HJ. Sequential surrogate modeling for efficient finite element model updating. Comput Struct 2016;168:30–45. https://doi.org/10.1016/j.compstruc.2016.02.005.